NMNAT2 supports vesicular glycolysis via NAD homeostasis to fuel fast axonal transport

Sen Yang
Indiana University Bloomington
Zhen-Xian Niou
Indiana University Bloomington
Andrea Enriquez
Indiana University Bloomington
Jacob LaMar
Florida Atlantic University
Jui-Yen Huang
Indiana University Bloomington
Karen Ling
Ionis Pharmaceuticals Inc
Paymaan Jafar-Nejad
Ionis Pharmaceuticals Inc
Jonathan Gilley
Cambridge University: University of Cambridge
Michael P. Coleman
Cambridge University: University of Cambridge
Jason M. Tennessen
Indiana University Bloomington
Vidhya Rangaraju
Max Planck Florida Institute for Neuroscience
Hui-Chen Lu (hclu@indiana.edu)
Indiana University Bloomington https://orcid.org/0000-0002-6628-7177

Research Article

Keywords:

Posted Date: May 19th, 2023

DOI: https://doi.org/10.21203/rs.3.rs-2859584/v1

Abstract

Background

Bioenergetic maladaptations and axonopathy are often found in the early stages of neurodegeneration. Nicotinamide adenine dinucleotide (NAD), an essential cofactor for energy metabolism, is mainly synthesized by Nicotinamide mononucleotide adenylyl transferase 2 (NMNAT2) in CNS neurons. NMNAT2 mRNA levels are reduced in the brains of Alzheimer's, Parkinson's, and Huntington's disease. Here we addressed whether NMNAT2 is required for axonal health of cortical glutamatergic neurons, whose long-projecting axons are often vulnerable in neurodegenerative conditions. We also tested if NMNAT2 maintains axonal health by ensuring axonal ATP levels for axonal transport, critical for axonal function.

Methods

We generated mouse and cultured neuron models to determine the impact of NMNAT2 loss from cortical glutamatergic neurons on axonal transport, energetic metabolism, and morphological integrity. In addition, we determined if exogenous NAD supplementation or inhibiting a NAD hydrolase, sterile alpha and TIR motif-containing protein 1 (SARM1), prevented axonal deficits caused by NMNAT2 loss. This study used a combination of genetics, molecular biology, immunohistochemistry, biochemistry, fluorescent time-lapse imaging, live imaging with optical sensors, and anti-sense oligos.

Results

We provide *in vivo* evidence that NMNAT2 in glutamatergic neurons is required for axonal survival. Using *in vivo* and *in vitro* studies, we demonstrate that NMNAT2 maintains the NAD-redox potential to provide "on-board" ATP via glycolysis to vesicular cargos in distal axons. Exogenous NAD^+ supplementation to NMNAT2 KO neurons restores glycolysis and resumes fast axonal transport. Finally, we demonstrate both *in vitro* and *in vivo* that reducing the activity of SARM1, an NAD degradation enzyme, can reduce axonal transport deficits and suppress axon degeneration in NMNAT2 KO neurons.

Conclusion

NMNAT2 ensures axonal health by maintaining NAD redox potential in distal axons to ensure efficient vesicular glycolysis required for fast axonal transport.

Background

Glucose is the primary energy source in the brain [1, 2]. Recent human studies highlight bioenergetic maladaptations in the brain during neurodegenerative disorders of aging (NDA) [3], such as Alzheimer's disease (AD). In AD, the brain's white matter [4], which comprises long-range axonal tracts, exhibits glucose hypometabolism. Axons, the longest and the most complex subcellular compartments of neurons [5–7], are particularly vulnerable to neurodegenerative conditions [8–10]. Two key questions concerning glucose metabolism in axons during NDAs include: Does glucose hypometabolism in long-range axons cause axonopathy, an early sign of neurodegeneration [11, 12]? And what are the key steps in maintaining axonal energetics to ensure axonal function and health?

Nicotinamide adenine dinucleotide (NAD) is a cofactor essential for energy metabolism. The ratio of oxidized (NAD^+) to reduced (NADH) form of NAD, named the NAD redox potential, is a pivotal driver of glycolysis, tricarboxylic acid (TCA) cycle, and oxidative phosphorylation (OXPHO) [13]. Nicotinamide mononucleotide adenylyl transferase 2 (NMNAT2) is the major NAD-synthesizing enzyme in CNS neurons [14–16] and is a key axonal maintenance factor [17–20]. mRNA levels of NMNAT2 are significantly reduced in the brains of AD, Parkinson's disease (PD), and Huntington's disease (HD) patients [21–23]. Notably, upregulating NMNAT2 and other NMNATs is protective in multiple neurodegenerative disease models [23, 24]. However, whether NMNAT2 maintains axonal health by contributing to axonal bioenergetics is not clear.

Previous studies showed that NMNAT2 is localized to Golgi-derived vesicles in axons and undergoes fast, bi-directional axonal transport in superior cervical ganglia neurons [25, 26]. Axonal transport between the cell body and axonal terminals is critical for neurotransmission, synaptic plasticity [27], and neuronal health [28]. To achieve fast and continuous movement of cargos along highly arborized axons across long distances [29–31], the bioenergetic machinery must be locally mobilized to provide ATP. It has been demonstrated that glycolytic enzymes specifically attach to fast-moving vesicular cargos to fuel fast axonal transport [32, 33]. Surprisingly, ultra-resolution electron microscopy studies find that mitochondria, the other potential energy source, in axons are often small in sizes and sparsely distributed [34, 35]. Moreover, *in vitro* evidence suggests glycolysis but not mitochondrial oxidative phosphorylation (OXPHO) supplies constant energy to fuel fast axonal transport [32]. Moving one vesicular cargo at physiological speed consumes ~ 200 ATP molecules per second [36], while each glycolytic cycle only yields 2 ATP molecules. Thus, vesicular glycolysis has to turnover rapidly to support fast axonal transport. In this study, we aimed to test the hypothesis that NMNAT2 maintains the NAD redox potential necessary to drive ATP synthesis through vesicular glycolysis for fast axonal transport.

We employed both animal (*in vivo*) and culture (*in vitro*) model systems to determine whether: (1) NMNAT2 is required for the health of long-range axons of glutamatergic neurons; (2) NMNAT2 is essential for fast axonal transport; (3) NMNAT2 ensures the proper NAD^+/NADH redox potential for glycolysis on vesicular cargos; and (4) NAD supplementation rescues the axonal phenotypes caused by NMNAT2 loss. Our results reveal the importance of NMNAT2 in maintaining axonal NAD redox potential and driving the onboard glycolysis necessary for fast axonal transport; we also demonstrate that NMNAT2 reduction increases the vulnerability of distal axons.

Methods

Mice

The generation of NMNAT2$^{f/f}$ mice carrying a Cre recombinase-dependent gene trap cassette within intron 1 of NMNAT2 gene has been described [37]. Here we generated NMNAT2 conditional knockout (cKO) mice by crossing NMNAT2$^{f/f}$ mice with NEX-Cre mice [38] to delete NMNAT2 in cortical glutamatergic neurons after embryonic day 11.5 (E11.5). NMNAT2 cKO mice were smaller and exhibited an ataxia phenotype with wobbling movements. Thus, 5 grams of DietGel 76A (Clear H_2O, Westbrook, ME, USA) were given daily after animals were weaned. NEX-Cre positive NMNAT2$^{f/+}$ and NMNAT2$^{+/+}$ and NEX-Cre negative NMNAT2$^{f/f}$ littermates were used as controls for NEX-Cre positive NMNAT2$^{f/f}$. The generation and genotyping of NMNAT2-Blad mice have been described previously [39]. In these mice, the NMNAT2 null mutation was generated by transposon-mediated gene-trap mutagenesis. Sarm1 KO (S^{null}/S^{null}) mice [40] were crossed with NMNAT2 cKO mice to generate cKO;S^{null}/+ and cKO; S^{null}/S^{null} transgenic mice. Littermate controls include NEX-Cre/+;NMNAT2$^{f/+}$;S^{null}/+, NMNAT2$^{f/+}$;S^{null}/+; NEX-Cre/+;NMNAT2$^{f/+}$;S^{null}/ S^{null}, and NMNAT2$^{f/f}$;S^{null}/ S^{null}. Both male and female mice were used for all experiments. All mice were housed under standard conditions with food and water provided ad libitum and maintained on a 12 h dark/light cycle. Mice were housed and used in compliance with the NIH Guidelines for the Care and Use of Laboratory Animals and were approved by the institutional animal care and use committees at Indiana University and Max Planck Florida Institute for Neuroscience.

Genotyping

For mice, ear lysates were prepared by immersing the tissue derived from a small ear clip in digestion buffer (50 mM KCl, 10 mM Tris–HCl, 0.1% Triton X-100, 0.1 mg/ml proteinase K, pH 9.0), vortexing gently, and then incubating for 3 h at 60°C to lyse the cells. For embryos, the same digestion buffer with 0.2 mg/ml proteinase K was used, and embryonic tail lysates were incubated at 60°C for 15 min with 1500 rpm shaking in a thermoshaker. These lysates were then heated to 95°C for 10 min to denature the proteinase K (Thermo Scientific, Rockford, IL, USA) and centrifuged at 16,100 g for 15 min. The supernatants were used as DNA templates for polymerase chain reactions (PCRs, EconoTaq Plus Green 2X mater mix, Lucigen, Middleton, WI, USA). For embryonic genotyping during primary culture preparation, a QIAGEN Fast Cycling PCR Kit was used. The sequences of the primers used for genotyping are listed in the reagent table. For NMNAT2$^{f/f}$ line: primers A and B detect WT allele; primers B and C detect NMNAT^{f} allele. For NEX-Cre line: primer Cre484 and Cre834 detect Cre positive allele. For the NMNAT2-Blad line: primers A and B detect WT allele, and primers R3 and Rf detect KO allele. For SARM1 KO line: primers WT-R and Sarm1-common detect WT allele, and primers Sarm1-common and Mut-R detect KO allele.

Immunohistochemistry for brain sections

Mice were anesthetized and perfused with 4% paraformaldehyde (PFA) in PBS. Brains were harvested, post-fixed with 4% PFA in PBS overnight at 4°C, and then rinsed with PBS. Free-floating brain sections

were prepared by sectioning these fixed brains into 40-µm-thick sections in the coronal plane with a Leica VT-1000 Vibrating microtome or Sliding Microtome SM-2000R (Leica Microsystems).

For immunohistochemistry, sections were permeabilized with 0.3% Triton X-100 in PBS for 20 min at room temperature, incubated with blocking solution (3% normal goat serum prepared in PBS with 0.3% Triton X-100) for 1 h, and then incubated with primary antibodies diluted in blocking solution overnight at 4°C. The next day, sections were washed with 0.3% Triton PBS 3 times and then incubated with the secondary antibodies diluted in blocking solution at 4°C for 2 h. After the incubation, samples were washed with 0.3% Triton PBS 3 times. Draq5 (1:10,000 dilution, Cell Signaling) or 4´,6-diamidino-2-phenylindole (DAPI, 5 µg/ml, Invitrogen) were added during the first wash step to visualize nuclei. Dako mounting medium was used to mount the brain sections.

Microscopy, imaging, and data analysis for brain sections.

Bright-field images were obtained with Zeiss SteREO Discovery.V8 Microscope (Carl Zeiss Microscopy). Confocal fluorescent images were taken by a Leica TCS SPE confocal microscope (Leica DM 2500) with a 10x objective lens (0.3 N.A.) or a 40x (0.75 N.A.) objective lens. Some confocal images were taken with a Nikon A1R laser scanning confocal (Nikon A1) with a 10x (0.5 N.A.) or a 60x (1.4 N.A.) oil objective lens. DAPI/Draq5 immunofluorescence was used to identify comparable anatomical regions across different brain sections. A minimum of three sections were imaged per mouse, and each anatomical region was imaged with both sides of the cortices, comparable across all animals. Images for particular staining were acquired with identical imaging parameters to minimize signal saturation in all experimental groups. The thickness of the corpus callosum was measured from the dorsal to ventral edges of NFM-positive axonal tracts in coronal plane brain sections. The thickness of the primary somatosensory cortex was measured from the pial surface to white matter regions using ImageJ “Straight” function. The total pixel values of APP signals and area sizes were measured by Image J to acquire APP signal densities.

NMNAT2 in situ hybridization

In situ hybridization on embryonic sections was done by the Baylor College of Medicine Advanced Technology Core Labs. The experiment was performed using a high-throughput automated platform. Cryostat sections of E14.5 embryos were placed on a standard microscope slide that was subsequently incorporated into a flow-through chamber. The chamber was then placed into a temperature-controlled rack, and the required solutions for pre-hybridization, hybridization, and signal detection reactions were added to the flow-through chamber with an automated solvent delivery system. Details can be found in a previous publication [5]. The RNA probe was generated using the Allen Brain Atlas database sequence. Images were acquired by a Leica CCD camera with a motorized stage. Multiple images were collected from the same section. Individual images were stitched together to produce a mosaic representing the entire section.

Primary cortical neuronal cultures

To culture NMNAT2 KO neurons, E15.5-16.5 embryos were harvested from NMNAT2-Blad heterozygous (HET) female mice mated to NMNAT2-Blad HET male mice. Embryos of both sexes were included for culture preparations. The cortical tissue of each embryo was dissected and then dissociated individually using the Worthington Papain Dissociation Kit (Worthington Inc.) according to the manufacturer's protocol. Genotyping was performed before the completion of papain dissociation. Cortices from multiple NMNAT2-Blad wildtype (WT) and HET embryos were combined as control group for dissociation and plating; the cortices from multiple NMNAT2-Blad homozygous embryos were pooled together as KO group for dissociation and plating. $NMNAT2^{f/f}$ neuron cultures were prepared from cortical tissue dissected from E15.5-16.5 $NMNAT2^{f/f}$ embryos harvested from $NMNAT2^{f/f}$ female mice mated with $NMNAT2^{f/f}$ male mice. After plating, cortical neurons were maintained in Neurobasal Media (Gibco™, ThermoFisher Scientific) supplemented with 2% B-27 (Gibco™), 2 mM GlutaMAX™ (Gibco™), and 100 U/ml penicillin-streptomycin (Gibco™), incubated at 37°C with 5% CO2 and appropriate humidity. One-third of the media was replenished every 3 days.

Immunocytochemistry and confocal imaging

About $2.5*10^5$ cortical neurons were plated on 12 mm diameter coverslips coated with poly-D-lysine (PDL) in 24-well plates ($1.3*10^3$ cells/mm^2). At indicated days *in vitro*, cortical neurons were first fixed by 4% PFA and 4% sucrose in PBS for 20 min, incubated for 60 min in blocking buffer (0.1% Triton X-100 and 5% Goat Serum in PBS), and then incubated with primary antibody containing blocking buffer overnight at 4°C on a gentle rotating platform. Samples were washed with 0.1% Triton in PBS 3 times and incubated with a secondary antibody containing blocking buffer for 2 h. After the incubation, samples were washed with 0.1% Triton in PBS 3 times. Coverslips were removed to mount with ProLong™ Gold antifade mounting medium with DAPI.

Fluorescent confocal images were taken by a Leica TCS SPE confocal microscope using a 63x (1.4 N.A.) oil objective lens or by a Nikon A1R-HD25 laser scanning confocal microscope with an Apo Lambda S 60x (1.4 N.A.) oil objective lens. Z-stack images were taken with 0.5 μm Z-step size to cover the whole depth of the cultured neurons. Images were acquired with identical imaging parameters chosen to optimize the signal-to-noise ratio and avoid saturated pixels in experimental groups. To quantify APP or TUJ1, 3–5 regions were randomly selected per coverslip for imaging. Each image accounts for one data point in quantification. Two coverslips per group were imaged for each batch of culture. To sample a larger area for imaging MAP2 and βIII-tubulin staining for gross neurite area quantification, the "large image stitching" function in Nikon NIS-Elements software with 5–10% overlap was used to tile 4 adjacent fields of view together as one image.

Quantification of APP accumulation and gross neurite area in neuronal culture

ImageJ was used for quantification of the maximum intensity projected images. APP signal in somata and dendrites was manually excluded, then the default threshold method was applied to select the top 10% tail of total pixels, and the "analyze particles" function was applied to select particles of area larger

than 0.9 μm^2 which were identified as “accumulated APP”. The total area of “accumulated APP” was calculated in each image to evaluate the phenotype. MAP2-positive areas were identified using an auto-thresholding method and measured for each image. A MAP2 positive area was selected by the “create selection” function after thresholding, then restored and deleted from the βIII-tubulin channel. Therefore, the remaining βIII-tubulin signal solely represented axonal regions. Similarly, mean threshold was applied to measure the βIII-tubulin positive area. Live cells were distinguished from dead cells by DAPI-stained nuclei morphology, and the number of live cells was counted for each image. MAP2 and βIII-tubulin areas were normalized by dividing by the live cell number in each image. We observed a skew in the data if the cell density dramatically differed between Ctrl and KO. Therefore, only images with a live cell number between 150 to 300 within 0.31 mm^2 image area (485–970 cells/mm^2) were used for the analysis.

Plasmid DNA constructs

pEGFP-n1-APP was a gift from Zita Balklava and Thomas Wassmer (Addgene plasmid # 69924; http://n2t.net/addgene:69924; RRID: Addgene_69924) [41]. pEGFP-c1-SNAP25, pEGFP-n1-SYPH, and pmCherry-n1-NMNAT2 were gifts from Michael Coleman and Jonathan Gilley [25]. pCX-EGFP was a gift from Matthew Neil Rasband [42]. pLV-mitoDsRed was a gift from Pantelis Tsoulfas (Addgene plasmid # 44386; http://n2t.net/addgene:44386; RRID: Addgene_44386) [43]. pcDNA3.1-SoNar and pcDNA3.1-cpYFP were gifts from Yang Yi [44]. pCMV-MitoVenus was a gift from Lulu Cambronne [45]. pCAG-mCherry was a gift from Ken Mackie. pcDNA3-Syn-ATP and pcDNA3-Cyto-pHluorin were from Vidhya Rangaraju [33].

Transfection in neuronal culture

For lentiviral transduction in $NMNAT2^{f/f}$ neurons, a lentivirus expressing copGFP or iCre under elongation factor 1 alpha (ELF1alpha) promoter was applied at 2 multiplicity of infection (MOI) at 9 days *in vitro* (DIV9).

For lipofectamine transfection, about $1.6*10^6$ cortical neurons were plated onto PDL (Poly-D-Lysine)-coated MatTek dish (P35G-1.5-20-C) ($1.66*10^3$ cells/mm^2). For APP-EGFP and SNAP25-EGFP transport imaging, cortical neurons were transfected 16 to 20 h prior to the time-lapse imaging experiments using Lipofectamine 3000 (Thermo) following manufacturer’s instruction. For MitoDsRed transport imaging, cortical neurons were co-transfected with pCX-EGFP and pLV-mitoDsRed 36 to 48 h before live imaging using Lipofectamine 3000. Before adding the DNA-lipofectamine mixture, half of the conditioned culture medium was removed and saved for later. Two hours after incubation with DNA-lipofectamine mixture, one-third of the remaining medium was removed, and 2 ml of culture medium (1:1 of conditional medium and fresh medium) was added back immediately. For live imaging, all culture medium was replaced by 2–3 ml of Hibernate E low fluorescence buffer (BrainBits) supplemented with 2mM GlutaMAX™ to maintain the ambient pH environment.

For magnetofection, about $2.56*10^5$ cortical neurons were plated onto the center of a PDL-coated coverglass region of MatTek dish (P35G-1.5-14-C) ($1.66*10^3$ cells/mm^2). For Syn-ATP imaging and Cyto-

pHluorin imaging, cortical neurons were transfected 24 h before imaging using Combimag (OZ biosciences) and Lipofectamine 2000 (Invitrogen) according to the manufacturer's instruction. Briefly, 0.5 µg DNA was incubated with 0.5 µl lipofectamine in 50 µl transfection medium (Neurobasal media supplemented with 2 mM Glutamax without B27 or antibiotics) for 5 min, then mixed with 0.5 µl Combimag diluted in another 50 µl transfection medium for 10 min. The DNA-lipofectamine-Combimag mixture was further diluted in 125 µl of transfection medium. Then, the conditioned medium from cultured neurons was harvested, and the neurons were immediately rinsed twice in a warm transfection medium. The transfection medium used for rinsing was removed, and 150 µl of DNA-lipofectamine-Combimag mixture was added to the neurons. Neurons were placed on a magnetic plate for 20 min inside a 37°C and 5% CO_2 incubator. After 20 min, neurons were rinsed once in a warm transfection medium and replaced with the previously harvested warm, conditioned medium.

Axonal transport time-lapse video microscopy and movie analyses

Live imaging of neuronal cultures was carried out using an Olympus OSR Spinning Disk Confocal microscope (CSU-W1, Yokogawa) connected to a Hamamatsu Flash 4 V2 camera. The temperature was maintained at 37°C by a Tokai Hit Stage Top Incubation system. For APP-EGFP and SNAP25-EGFP transport recording, movies were taken in axonal segments at least 400 µm away from the soma (defined as distal axon) and axonal segments within 200 µm of the soma (defined as proximal axon) and captured at a rate of 5 frames/s for a total recording time of 60 s with a 63x oil objective (1.46 N.A.). For MitoDsRed transport imaging, neurons were co-transfected with EGFP, and the distance from an axonal segment of interest to soma was determined in the GFP channel under the eyepiece. Mitochondria transport videos were taken in the distal region at a 3-second time interval for a total recording time of 15 min with a 63x oil objective (1.46 N.A.). A z-stack with 1 to 1.5 µm z-step size was taken for each time point to cover all the mitochondria within the imaged axonal segment.

Kymographs were generated using ImageJ (http://rsb.info.nih.gov/ij) with "Velocity_Measurement_Tool" macro (http://dev.mri.cnrs.fr/projects/imagej-macros/wiki/Velocity_Measurement_Tool). Velocity quantification was manually performed by following the trajectory of each particle with an angle larger than 0° relative to the time axis. Stationary and repetitive bidirectional-moving particles were excluded for velocity measurements. If an anterograde or retrograde moving particle stopped briefly during the imaging and then continued moving, the paused portion was included in the velocity calculation. Although a portion of the axon could be out of focus, resulting in a discontinuous trajectory, the discontinuous trajectory was still traced as the same if the slope and timing matched. All the traced trajectories were saved in "ROI manager" in ImageJ. Particles that remained stationary or underwent repetitive bidirectional movements for most of the recording time were defined as stationary/dynamic pause events. Each trajectory of stational/dynamic pause particles that could be visually separated was included in the number of stationary/dynamic pause events. The number of anterograde or retrograde events was counted in the same way. The stationary/dynamic pause percentage was calculated as the

number of stationary/dynamic events divided by the sum of the number of anterograde, retrograde, and stationary/dynamics pause events. Anterograde and retrograde percentages were calculated similarly.

Colocalization analysis

Control neurons were plated at a density of $1.8*10^3$ cells/mm^2 on PDL-coated 12mm diameter coverslip in 24-well culture plate (about $3.5*10^5$ cells on 190 mm^2 surface). Through transfection, pmCherry-n1-NMNAT2 was co-expressed with pEGFP-n1-APP, pEGFP-n1-SYPH, and pEGFP-c1-SNAP25 at DIV6, and samples were fixed using 4% PFA with 4% sucrose dissolved in PBS at DIV8. Immunocytochemistry was conducted to amplify the mCherry and EGFP signals after fixation. ProLong™ Gold antifade mounting medium with DAPI was used to mount the coverslips. Fluorescent confocal images were taken by a Leica TCS SPE confocal microscope using a 63x (1.4 N.A.) oil objective lens with a system-optimized z-step size. The colocalization was further validated by structure illumination imaging using OMX-SR 3D-SIM Super-Resolution System with a 60x (1.516 N.A.) oil objective lens, following system-optimized z-step size.

JACoP (Just Another Colocalization) ImageJ plugin was used to analyze confocal images. Briefly, cell debris signal outside axon was manually deleted. “Objects based methods” was used. The threshold for both channels was manually adjusted based on the visual judgement of signal coverage. The minimum particle size was set as 25 pixels. The ratio of particles colocalized to NMNAT2 was calculated as the number of colocalizing particles in APP, SYPH, or SNAP25 channels divided by the total number of particles in these channels.

Mitochondria density and morphology analysis

Both control and KO neurons were plated at a density of $1.8*10^3$ cells/mm^2 on PDL-coated 12mm diameter coverslip in 24-well culture plate (about $3.5*10^5$ cells on 190 mm^2 surface). Neurons were co-transfected with pCMV-MitoVenus and pCAG-mCherry at DIV6 and fixed using 4% PFA with 4% sucrose at DIV8. Immunocytochemistry with antibodies against GFP (Chicken) and RFP (Rabbit) was conducted to immuno-amplify the MitoVenus and mCherry signals after fixation. ProLong™ Gold antifade mounting medium with DAPI was used to mount the coverslips.

Images were taken by a Nikon A1 laser scanning confocal microscope using a 1.4 N.A. Apo Lambda S 60x oil objective lens with 0.171 µm z-step size and 3 times zoom to cover the whole depth of the axon segment of interest. Axonal segments at least 400 µm away from the soma were identified in the RFP channel and selected for imaging. Distal axons from at least 8–10 neurons were randomly sampled per coverslip and two coverslips were imaged per group. Images were analyzed using Imaris (Oxford Instruments). RFP channel was used to generate the surface masking of the axonal region, within which the MitoVenus signal was used to create the surface representing mitochondrial morphology. To calculate mitochondria density, length of the axon segment in each image was measured. Density was calculated from mitochondria number divided by axonal length in each image. Sphericity values of mitochondrial surface from axon segments of each individual neuron were input in each column in the

column table in Prism 9.0 (each column representing one individual neuron). Cumulative frequency distribution of relative percentage was generated through “column analysis” function in Prism 9.0. Statistical analysis of cumulative frequency distribution is described in “quantification and statistical analysis” section.

NAD^+/NADH-Glo™ bioluminescent assay

Control or KO neurons were cultured in a 96-well plate at a density of $1.3*10^3$ cells/mm^2 ($4.235*10^4$ cells onto 32 mm^2 surface). Following manufacturer’s instruction (Promega), neuronal cultures at DIV8 were washed three times with PBS and lysed in buffer containing 25 µl PBS and 25 µl 1% DTAB (Dodecyl trimethyl ammonium bromide) base buffer (100 mM Sodium Carbonate, 20 mM Sodium Bicarbonate, 10 mM Nicotinamide, 0.05% TritonX-100, pH 10–11). 30 µl of lysate was collected for BCA protein assay. 20 µl of the remaining lysate was diluted into 105 µl. 50 µl of diluted lysate was mixed with 25 µl 0.4 N HCl and incubated at 60°C for 15 min to detect NAD^+, while another 50 µl of diluted lysate (without 0.4 N HCl) was incubated at 60°C for 15 min to detect NADH. After incubation, 25 µl of 0.5 M Tris base was added to the wells used for detecting NAD^+ to neutralize the HCl; 50 µl of a solution containing 1:1 0.4 N HCl and 0.5 M Tris base was added to wells used for detecting NADH. Freshly dissolved NAD^+ in PBS was used to prepare the standard curve. Luminescent signal from each sample was converted into absolute NAD^+ or NADH concentration and normalized to protein concentration measured by the BCA method (Thermo Scientific™).

NAD^+/NADH live imaging using the genetically encoded sensor, SoNar

Around $1.66*10^3$ cells/mm^2 cortical neurons were plated on PDL (Poly-D-Lysine)-coated MaTek dish (P35G-1.5-20-C). The NAD^+/NADH sensor, SoNar, and its control cpYFP were gifts from Yi Yang’s group. On DIV6, 2.5 ug DNA of pCDNA3.1-SoNar or pCDNA3.1-cpYFP were transfected. After 48 h expression of the sensor or control (DIV8), the culture medium was replaced by Hibernate E buffer and maintained at 37°C for imaging using a Leica TCS SP8 confocal laser scanning platform with HyD hybrid detector and an HC PL APO 40x (1.2 NA) water-immersion objective. The SoNar sensor/cpYFP was excited at 440 nm and 488 nm, and the emission at 530+/-15 nm was detected to obtain the ratiometric measurement. Laser power intensity was maintained the same between WT/Het and KO in the same experiment. Axonal segment > 400 µm away from the soma (defined as distal axon) and axonal segment within 200 µm from the soma (defined as proximal axon) were imaged with 1 µm z-step size to cover the whole axon segment within the field of view. Maximum intensity projection was generated for further analysis. Mean grey value from 488 nm excitation (F488) and 440 nm excitation (F440) was measured in ImageJ using manually drawn regions of interest (ROIs) that circle the edges of the axons of interest. Five rectangular ROIs were randomly drawn in the background area and the average mean grey value from these five ROIs was used to subtract background. After background subtraction, the ratio was calculated as ($F488_{axon}$-$F488_{background}$)/ ($F440_{axon}$-$F440_{background}$). Data presented were normalized to control as a percentage.

Syn-ATP live imaging

Syn-ATP imaging was performed using a custom-built inverted spinning disk confocal microscope (3i imaging systems; model CSU-W1) with two cameras: an Andor iXon Life 888 for confocal fluorescence imaging and an Andor iXon Ultra 888 electron-multiplying charge-coupled device camera for luminescence imaging. The Andor iXon Ultra 888 camera was selected for ultralow dark noise, further reduced by cooling to − 100°C. The Andor iXon Ultra 888 camera speed used for luminescence measurements was 1 MHz with 1.00 gain and 1000 intensification. Image acquisition was controlled by Slidebook 6 software. Confocal imaging of mCherry fluorescence was performed by illuminating neurons with a 561 nm laser with 200 ms exposure and 2.3 mW laser power. For mCherry fluorescence measurements, ten frames of timelapse imaging without interval were acquired and the average of ten images was used to measure the mCherry fluorescence signal from the varicosities of interest. For luminescence measurements, luminescence photons were collected by accumulating the image for 60 s in the presence of 2 mM D-luciferin (Promega), and the luminescence signal was measured from the same varicosities as the corresponding fluorescence image. All images were acquired through a Plan-Apochromat 63x/1.4 N.A. Oil objective, M27 with DIC III prism, using a CSU-W1 Dichroic for 561 nm excitation with Quad emitter and individual emitters for confocal fluorescence, and a 720 nm multiphoton short-pass emission filter was used for luminescence. During imaging, the temperature was maintained at 37°C using an Okolab stage top incubator with temperature control. Distal axons at least 400 µm from the soma were selected for imaging.

Images were analyzed in ImageJ using the plugin Time series analyzer (https://imagej.nih.gov/ij/plugins/time-series.html). Regions of Interest (ROIs) of ∼1.2 µm diameter were drawn around the varicosities of interest to obtain the mean fluorescence and luminescence values from the corresponding fluorescence and luminescence images. We observed that some presynaptic varicosities in DIV8 neurons are not mature and not stable over the time course of imaging and have a heterogenous amount of synaptophysin expression, consistent with previous studies [46]. Therefore, we focused on varicosities of at least 1.2 µm diameter, stable during the 60s luminescence acquisition. Neurons with an average mCherry fluorescence value lower than 1000 A.U. in their varicosities were excluded from the analysis, as a low fluorescence value indicates low expression of the sensor, resulting in low luminescence signal-to-noise ratio. For background subtraction of the fluorescence and luminescence values, three rectangular ROIs were drawn in the background region surrounding axons of interest. The average mean values from these background regions in the fluorescence ($F_{background}$) and luminescence ($L_{background}$) channels were used to subtract the background for each varicosity from the fluorescence ($F_{varicosity}$) and luminescence ($L_{varicosity}$) channels, respectively.

$$\frac{L}{F} = (L_{varicosity} - L_{background})/(F_{varicosity} - F_{background})$$

The average L/F value across varicosities within one neuron was used to represent that neuron's relative presynaptic ATP level, accounting for one data point in the statistical analysis.

pH measurement and pH correction of L/F measured from Syn-ATP

Cytoplasmic pHluorin (Cyto-pHluorin) was transfected in cortical neurons at DIV7, and imaging was done at DIV8 using the same equipment setting as Syn-ATP measurements. Detailed procedures are described in the previous publication [33]. In brief, neuronal culture medium was replaced by Tyrodes buffer containing (in mM) 119 NaCl, 2.5 KCl, 2 $CaCl_2$, 2 $MgCl_2$, 30 HEPES (buffered to pH 7.4 at 37°C), and 25 glucose. Basal fluorescence intensity of Cyto-pHluorin was monitored for 5 min, acquired every 15 s (20 timepoints). ROIs were drawn around the axonal segment of interest and the mean fluorescence value was measured over the 20 timepoints ($F_{axon,\ frame\ i}$). Three rectangular ROIs were drawn in the background region surrounding the axon to measure the average background value across the 20 timepoints ($F_{background,\ frame\ i}$). F_{basal} was calculated by subtracting background in each timepoint and then averaging the value across the 20 timepoints.

$$F_{basal} = \frac{\sum_{20\ frames}(F_{axon,\ frame\ i} - F_{background,\ frame\ i})}{20}$$

Then, 1 μM Oligomycin was added to the Tyrodes buffer and incubated for 5 min. Fluorescence of Cyto-pHluorin was imaged to obtain F_{Oligo} using the above calculation.

Then, Tyrodes buffer was replaced by an NH_4Cl solution containing (in mM) 50 NH_4Cl, 70 NaCl, 2.5 KCl, 2 $CaCl_2$, 2 $MgCl_2$, 30 HEPES (buffered to pH 7.4 at 37°C), and 25 glucose. The response of Cyto-pHluorin to NH_4Cl treatment was monitored for 5 min every 15 s (20 timepoints). The measured fluorescence of Cyto-pHluorin was called F_{Max} and was background subtracted, as explained above.

Cytosolic pH of the basal and Oligomycin treatments were determined using the following modified Henderson-Hasselbalch equation:

$$pH_{Basal} = \text{pKa} - \log[(\frac{1+10^{pKa-7.4}}{\frac{F_{Basal}}{F_{Max}}}) - 1] \qquad pH_{Oligo} = \text{pKa} - \log[(\frac{1+10^{pKa-7.4}}{\frac{F_{Oligo}}{F_{Max}}}) - 1]$$

$$pKa = 7.1 \; for \; CytopHluorin$$

From the known pH values at various conditions, Syn-ATP L/F value was corrected as follows:

$$L_1 \sim Luminescence \; under \; pH_1 \qquad L_0 \sim Luminescence \; under \; pH_0$$

$$pH_1 = \text{pKa} - \log[(\frac{1+10^{pKa-pH_0}}{\frac{L_1}{L_0}}) - 1]$$

$$L_0 = L_1 * (\frac{1+10^{pKa-pH_1}}{1+10^{pKa-pH_0}}) \qquad pKa = 7.03 \; for \; SynATP$$

Here, the average pH in each condition was used for correction and we did not propagate errors in pH measurements into the final error shown in L/F measurements. pH corrections of L/F values were only done for those conditions that showed a statistically significant change in pH compared to control (as in Fig. 5-S1).

NAD$^+$ supplementation in neuronal culture

NAD$^+$ (Roche, NAD100-RO) was dissolved in PBS at a stock concentration of 100 mM, sterilized, aliquoted, and stored at -80°C. Only less than 1-week-old stocks were used. On the starting day of supplementation, NAD$^+$ was applied to the culture medium at a final concentration of 1 mM. In the following days before live imaging, 1/3 of culture medium was replaced with a fresh medium containing 1 mM NAD$^+$ daily. 1 mM NAD$^+$ was supplemented to the Hibernate E low fluorescence buffer used for live imaging. In the following days before fixation, 1/3 of culture medium was replaced with fresh medium containing 1 mM NAD$^+$ every 3 days.

2-Deoxyglucose (2DG) treatment in neuronal culture

To acutely inhibit glycolysis while leaving mitochondrial respiration intact, 15 mM 2-DG and 10mM methyl-pyruvate were added to the customized Hibernate E low fluorescence buffer containing 0 mM glucose (~ 262 mmol/kg osmolality). Culture medium was replaced by the 2DG Hibernate E buffer, and neurons were incubated for 30 min before imaging APP-EGFP axonal transport. For each culture dish, imaging of axonal transport was conducted within 30 min of 2DG treatment. To chronically inhibit glycolysis, 25 mM 2-DG and 10 mM methyl-pyruvate were added to the neurobasal medium containing 25 mM glucose. 2 days after treatment, neuronal culture was fixed for immunocytochemistry.

Oligomycin treatment in neuronal culture

To acutely inhibit ATP synthesized from mitochondrial respiration, 1 μM oligomycin was added to the commercial Hibernate E low fluorescence buffer containing 25 mM glucose (~ 241 mmol/kg osmolality).

Culture medium was replaced by Oligo Hibernate E buffer, and neurons were incubated for 5 min before imaging APP-EGFP axonal transport, Syn-ATP, or Cyto-pHluorin. For each culture dish, live imaging was conducted within 30 min of oligomycin treatment. For APP axonal transport imaging, oligomycin (Calbiochem 495455) was dissolved in DMSO to prepare a 1 mM stock. For Syn-ATP and Cyto-pHluorin imaging, oligomycin (Sigma-Aldrich O4876) was dissolved in 100% Ethanol to prepare a 1 mM stock.

Antisense Oligonucleotide (ASO) treatment in neuronal culture

The antisense oligonucleotides (ASOs) were designed, synthesized, and preliminarily tested by Ionis Pharmaceuticals. ASOs consist of 20 chemically modified nucleotides with a central gap of 10 deoxynucleotides flanked on its 5' and 3' sides by five 2'-O-(2-methoxyethyl) (MOE)-modified nucleotides. Thirteen of the phosphodiester internucleotide linkages were replaced with phosphorothioate to further enhance the stability of ASOs to endogenous nucleases. The non-targeting ASO, 5’-CCTATAGGACTATCCAGGAA-3’ (ASO30), was used as a control. The ASOs targeting mouse SARM1 mRNA, 5’-GGTAAGAGCCTTAGGCACGC-3’ (ASO33) and 5’-CCACCTTTTAGTCAAGACCC-3’ (ASO47) were applied to silence SARM1 expression. Both ASOs arrived as 100mg/ml stock. On the treatment starting day, as indicated, ASOs were diluted into 5 μM as the final concentration in neuronal culture medium. In the following days before live imaging or fixation, 1/3 of culture medium was replaced with fresh medium containing 5 μM ASOs every 3 days.

Quantitative real-time PCR

Following ASO treatment, total RNA was extracted from neuronal culture by RNeasy Mini Kit (Qiagen 74104) and followed by on-column DNase digestion according to the manufacturer’s instructions. RNA concentration and purity was measured by NanoDrop 2000 spectrophotometer (ThermoFisher Scientific). 500ng RNA was used as input for cDNA synthesis through iScript™ advanced cDNA synthesis kit (Bio-Rad 1725038) following the manufacturer’s protocol. To quantify mRNA level, quantitative real-time PCR was conducted using PrimeTime™ Gene Expression Master Mix (IDT 1055772) following the manufacturer’s instruction.

To detect SARM1 mRNA, 0.3 ul of cDNA was loaded into the reaction mix (10 ul in total) containing 450 nM of SARM1 forward primer, 450 nM of SARM1 reverse primer, and 150 nM SARM1 probe. Mouse SARM1 primer-probe set was customized through PrimeTime™ qPCR Probe Assays (IDT). SARM1 forward primer sequence is 5’ TTTGTCCTGGTGCTGTCTG 3’. SARM1 reverse primer sequence is 5’ GCCACTCAAAGCCATCAATG 3’. SARM1 probe sequence is 5’ ACAATCTCCTTGTGCACCCAGTCC 3’, with FAM reporter at 5’, internal ZEN quencher, and 3’ Iowa Black® FQ quencher. To detect GAPDH mRNA as the internal control for normalization, 0.3 ul of cDNA was loaded into the reaction mix (10 ul in total) containing 500 nM of GAPDH forward primer, 500 nM of GAPDH reverse primer, and 250 nM GAPDH probe. Mouse GAPDH primer-probe set was acquired from PrimeTime™ Predesigned qPCR Assays with same reporter and quencher (Assay ID: Mm.PT.39a.1). These assays were run in QuantStudio 7 Flex Real-Time PCR Systems (ThermoFisher Scientific). The Ct value was defined as the number of cycles required

for the fluorescence to exceed the detection threshold. The ΔCt values were calculated by subtracting Ct value of GAPDH from SARM1. The ΔΔCt values were calculated by subtracting the average ΔCt of non-targeting ASO-treated control from the ΔCt of each sample. The relative fold change was calculated as $2^{-\Delta\Delta Ct}$.

Western blotting

Following ASO treatment, neuronal culture was lysed in RIPA buffer [20 mM of Tris-base, 150 mM of NaCl, 2 mM EDTA, 1% Triton X-100, 0.5% sodium deoxycholate, 0.1% sodium dodecyl sulfate (SDS), 1x cOmplete™ protease inhibitor cocktail and phosphatase inhibitor cocktail, pH 7.4], and homogenized by motorized disposable pellet mixers for 15 s, then sonicated by VMR Branson Sonifier 250 10 times under the parameter: duty cycle 30 and output 3.

Protein concentration was measured using the BCA method (Thermo Scientific™). 10–15 ug proteins were separated on a 10% SDS-polyacrylamide gel and then transferred to a nitrocellulose membrane of 0.45 μm pore size (BioRad). To detect SARM1 protein level, the membranes were incubated overnight with the homemade primary antibody against SARM1, a gift from Dr. Yi-Ping Hsueh [47]. The next day, the membranes were incubated with a species-appropriate secondary antibody. Western blot images were acquired by LI-COR Odyssey scanner and software (LI-COR Biosciences, Lincoln, NE USA) and quantified with NIH ImageJ software.

TUJ1 fragmentation quantification

Fluorescent confocal images of TUJ1 staining were taken as described in the "immunocytochemistry and confocal imaging" section. TUJ1 fragmentation was analyzed following the degeneration index measurements method described by Kraemer *et al.* [48], with some modifications to their particle size and circularity indexes. TUJ1 fragmentation quantification was performed using ImageJ. The fluorescent channel corresponding to TUJ1 was isolated and converted to a binary image using the "Make Binary" function, and this image was used for all subsequent steps of the analysis. The total TUJ1 expression area was measured using the "Measure" function. Images were then processed using the "Analyze Particles" function, setting the size parameter at 0.327 μm^2-817.587 μm^2 (4-10000 pixels) and circularity at 0.2-1. The area of selected particles was recorded and normalized to total area of TUJ1.

Experimental Design

No statistical methods were used to predetermine the sample size. For *in vivo* studies, investigators were blinded to the mouse genotype during data acquisition and analysis. For *in vitro* manipulation, investigators were not blinded to the genotype of neuronal cultures and treatments. While quantifying APP accumulation area, TUJ1 area, MAP2 area, TUJ1 fragmentation degree, and the analysis of axonal transport, investigators were blinded to each image's genotype and treatment information. For NAD/NADH-Glo™ bioluminescent assay, investigators were not blinded, and quantification was done by plate-reader without human curation. During the acquisition and quantification of NAD^+/NADH (SoNar) sensor imaging, Syn-ATP sensor imaging, and Cyto-pHluorin imaging, the investigators were not blinded

to the genotype and treatment of each image. Inclusion and exclusion criteria were applied during the analysis of Syn-ATP imaging to avoid varicosities with extremely low mCherry fluorescence (an indicator of low sensor expression). For Western Blotting and qPCR, investigators were not blinded to genotype and treatment. Except for gross neurite area measurement at DIV5 & DIV14 and Cyto-pHluorin live imaging, all experiments were replicated with culture from at least 2 independent primary culture preparations, as detailed in the supplementary Excel sheets.

Quantification/statistical analysis and figure constructions

Images were analyzed using Fiji (Image J with updated plug-ins) and Imaris. NAD/NADH-Glo™ bioluminescent Assay were measured by CLARIOstar plate reader. GraphPad Prism 9.0 (GraphPad Software) was used for statistical analysis. The outliers were detected by “ROUT” method in GraphPad Prism 9.0 and excluded for statistical analysis. The normality of residuals was mostly checked by D'Agostino-Pearson normality test as recommended by the GraphPad Prism user guide. For data with normally distributed residuals, one-way ANOVA, two-way ANOVA, or unpaired student’s t-test was used. For data that did not pass the D'Agostino-Pearson test, one-way ANOVA was replaced by Kruskal-Wallis test; two-way ANOVA was replaced by Multiple Mann-Whitney test or re-formatted for Kruskal-Wallis test; unpaired student’s t-test was replaced by the Mann-Whitney test.

To analyze cumulative frequency distribution curve, the dependent variable P (the relative percentage within each bin generated by GraphPad Prism “Column analysis”) was transformed into log(P/(100-P)) so that the relationship between covariate (bin of sphericity) and the transformed dependent variable was linearized. Then, a linear mixed model with a random slope and intercept was generated by SPSS using a restricted maximum likelihood approach to compare statistical difference between control and KO. The criterion for statistical significance was set at $p < 0.05$ for all statistical analyses.

Figures were made with Adobe Photoshop CS6 and Illustrator CS6, and brightness/contrast, orientations, and background corrections were applied to better illustrate the staining patterns.

Results

Deleting NMNAT2 in post-mitotic cortical glutamatergic neurons results in deformed brains and age-dependent loss of long-range cortical axons

Germline deletion of NMNAT2 in mice results in premature death at birth with severe axonal outgrowth deficits and subsequent degeneration in peripheral and optic nerves [37, 39]. Using explant cultures prepared from NMNAT2 KO embryonic cortices, Gilley *et al.* showed NMNAT2 KO cortical axons were shorter than control axons and exhibited degenerative phenotypes [37]. The premature death of germline NMNAT2 KO prevented *in vivo* examinations of the role of NMNAT2 in cortical neurons. Using mRNA *in situ* hybridization, we found that *nmnat2* mRNA is enriched in the embryonic cortical plate, where post-mitotic glutamatergic neurons are located (Fig. 1-S1A). Axons of cortical glutamatergic neurons often travel long distances to the contralateral hemisphere or subcortical regions via extensive and complex

arbors [6]. These observations led us to hypothesize that NMNAT2 is required for axonal outgrowth and the health of cortical glutamatergic axons.

To test this hypothesis, we generated NMNAT2 conditional knockout mice (cKO) by crossing NMNAT2 conditional allele mice ($NMNAT2^{f/f}$) [37] with a Nex-Cre transgenic mouse line, which expresses Cre recombinase in post-mitotic glutamatergic neurons mainly in the cortex and hippocampus from embryonic day 11.5 (E11.5) [38] (Fig. 1-S1B). Despite the restricted deletion of NMNAT2, only about 50% of cKO mice survived after birth, with no apparent lethality at E18.5 (Fig. 1-S1C-D). The surviving cKO mice weighed significantly less than their littermate controls from early postnatal ages through adulthood (Fig. 1A). NMNAT2 cKO mice exhibited evident hindlimb clasping (Fig. 1B), ataxia and forelimb circling phenotypes (10 out of 10 mice examined), reflecting motor behavioral deficits similar to those observed in many neurodegenerative mouse models [49–51]. cKO brains were visibly smaller than controls from postnatal ages (Fig. 1C). To evaluate gross brain morphology, we examined brain sections along rostral to caudal coronal planes with bright field microscopy. Compared to the brains of littermate controls, the brains of cKO mice displayed enlarged ventricles, smaller hippocampi, aberrant anterior commissures, a thinner corpus callosum, and a thinner cortex (Fig. 1D). We measured the thickness of the primary somatosensory cortex and found that it was significantly reduced in cKO compared to their littermate controls at postnatal day 16/21 (P16/21) and P90 (Fig. 1E). The degenerative brain phenotypes observed in NMNAT2 cKO brains highlight the importance of NMNAT2 in cortical neuronal health.

To distinguish whether brain dystrophy in NMNAT2 cKO is caused by axonal outgrowth deficits versus axonal maintenance failures, we examined the corpus callosum, where the long-range callosal axons of cortical glutamatergic neurons cross the midline on the way to their contralateral targets [8, 9]. To facilitate visualization of the corpus callosum, we immunostained the medium-size neurofilament (NF-M), a cytoskeleton protein enriched in axons, in P4/5, P16/21, and P90 cKO and control brains. There was no difference in corpus callosum thickness between control and cKO brains at P4/5 (Fig. 1F-G). However, a drastic reduction of corpus callosum thickness in cKO mice occurred by P16/21 and persisted until at least P90, the eldest age examined (Fig. 1F-G). Most callosal axons have already finished midline crossing at P4/5 [52, 53]. Thus, the normal corpus callosum thickness in cKO mice at P4/5 suggests that NMNAT2 deletion in glutamatergic neurons does not impair initial axonal outgrowth. Instead, the age-dependent reduction of corpus callosum thickness and degeneration-like brain morphology suggest that NMNAT2 is required to maintain the health of long-range cortical axons.

NMNAT2 loss leads to APP accumulation in axons prior to degeneration in vivo **and** in vitro

Based on the axon degeneration phenotype in NMNAT2 cKO brains, we hypothesized that NMNAT2 loss disrupts axonal physiology, ultimately resulting in axonal degeneration. Axonal transport plays a critical role in neuronal function and survival [28] and its deficits are thought to be a primary cause of axonopathy [54]. Amyloid Precursor Protein (APP) is rapidly and bidirectionally transported in axons [55–59] and is required for synaptogenesis and synaptic function, plasticity, etc. [60–62]. Axonal APP

accumulation has been found in AD mouse models [63, 64] and traumatic brain injury [65, 66], and serves as a marker for axonal transport breakdown [67].

To examine whether NMNAT2 deletion results in axonal transport deficits, we immunostained APP in brains prepared from P5 and P21 cKO mice and littermate controls. We found significant APP accumulation in the corpus callosum at P5 in cKO but not in control (Fig. 2A, E). This P5 timepoint is before the corpus callosum thickness is affected by NMNAT2 loss. In addition, we observed APP accumulation in cKO mice in brain regions where glutamatergic axons transit, including the hippocampal fimbria and striatum. In contrast, little APP signal was detected in the corresponding regions of control brains (Fig. 2B, C, E). At P21, where significant axon degeneration occurs, we found a striking buildup of the APP signal in areas enriched with long-range axons. As APP accumulations are encapsulated by myelin basic protein (MBP), a marker for myelinated axons, in the corpus callosum (Fig. 2D), it suggests that the APP aggregates are present in axons.

Interestingly, we also found analogous APP accumulations in the neurites of cortical neuron cultures prepared from NMNAT2 null (NMNAT2-Blad [39]) embryos, but not in wildtype or heterozygous (control) neurons after 8 days *in vitro* (DIV; Fig. 2-S1&S2). Immunostaining showed APP accumulation in axons labeled by βIII-tubulin/TUJ1 antibody but not in MAP2-positive dendrites of KO neurons (Fig. 2-S1C, D). APP accumulation increased drastically in KO axons from DIV8 to 14 (Fig. 2-S1A, B), while the signal densities for TUJ1 and MAP2 levels were similar between KO and control neurons (Fig. 2-S2A, B). Additionally, we detected fragmented and aggregated TUJ1 signal as a sign of axon degeneration at DIV14 (Fig. 2-S1 and Fig. 8-S2C). As our cortical neuronal cultures are prepared from E15.5/E16.5 embryonic cortex, by DIV8, they likely correspond to the first postnatal week of age *in vivo*. Additionally, we found significant axonal APP accumulation in NMNAT2-deleted cortical neurons using an alternative Cre-loxP approach (Fig. 2-S3). This *in vitro* recapitulation of APP accumulation and axon degeneration-like phenotype seen *in vivo* justifies using cultured NMNAT2 KO neurons as a cellular model to elucidate the molecular mechanisms mediating NMNAT2's function in axonal health.

NMNAT2 is required for the transport of fast-moving vesicular cargos in distal axons

As APP accumulation is observed prior to axonal degeneration in NMNAT2 KO axons, we hypothesized that NMANT2 is required for axonal transport. Previous work showed that NMNAT2 is localized to Golgi-derived vesicles and undergoes fast, bi-directional axonal transport in PNS axons [25, 26]. We observed a similar transport of NMNAT2 along axons and its colocalization and comigration with fast-moving cargos in cultured cortical neurons (Fig. 3-S1).

To determine whether NMNAT2 is required for axonal transport, we used time-lapse imaging to quantify axonal transport of EGFP-tagged vesicular cargos, APP and SNAP25, and DsRed-tagged mitochondria in control and NMNAT2 KO neurons at DIV6 and 8 (Fig. 3 and Fig. 3-S2). APP is a component of Rab5-containing vesicles [68], while SNAP25 is a component of Piccolo-bassoon transport vesicles [69]. Rab5

and SNAP25 undergo fast, bidirectional axonal transport [70, 71] mediated by kinesin-1 and dynein motor proteins [55, 72]. Distinct from vesicular cargos, axonal mitochondria move slowly and intermittently in both directions [73, 74], responding to the interplay between adaptor and motor proteins [75, 76]. To transfect only a few neurons with APP-EGFP, SNAP25-EGFP, or mito-DsRed expressing construct, lipofectamine transfection was conducted < 20 h before live imaging to reduce toxicity of overexpression. Such sparse labeling allowed us to identify distal (> 400 μm away from the soma) or proximal (within 200 μm of the soma) axon segments (Fig. 3-S3). Axonal transport of APP and SNAP25 was measured in distal and proximal segments (Fig. 3 and Fig. 3-S2). At DIV8, significant deficits in APP and SNAP25-transport were detected in KO distal segments (Fig. 3) but not proximal segments (Fig. 3-S2). Furthermore, we observed a substantial increase in the percentage of vesicles in the stationary and dynamic pause phases (Fig. 3C, F), a concomitant decrease in the percentage of vesicles engaging in anterograde movement, and reduced velocities in anterograde and retrograde directions (Fig. 3D, G). However, at DIV4 (data not shown) and 6 (Fig. 3C, D, F, G), APP and SNAP25 transport were unaffected in KO axons. In contrast to vesicular transport, mitochondrial distribution, morphology, and motility were unaffected in KO neurons at DIV8 (Fig. 3-S4), despite the heterogeneous mitochondrial velocities reported previously [77]. These results demonstrate that NMNAT2 is required for fast transport of vesicular cargos but not mitochondria, and that NMNAT2 loss affects distal axon transport before axon degeneration.

NMNAT2 maintains global NAD, NADH levels, and local NAD/NADH redox potential in distal axons

NMNAT2 catalyzes NAD synthesis in the salvage pathway, the major pathway in CNS neurons for NAD biosynthesis [15]. The ratio of oxidized (NAD^+) to reduced (NADH) forms of NAD establishes the NAD redox potential (NAD^+/NADH) and is crucial to driving glucose metabolism [78, 79]. To determine if NMNAT2 is required for maintaining the NAD redox potential, we measured the abundance of NAD^+ and NADH at DIV8, when axonal transport deficit first becomes evident in KO axons (Fig. 2-S1 C,D). Both NAD^+ and NADH levels were reduced to ~ 50% of their control value in KO neurons, suggesting that NMNAT2 is a major source of NAD in cortical neurons. However, since NAD^+ and NADH levels were reduced to the same extent upon NMNAT2 loss, the NAD redox potential measured from whole neurons remained unchanged (Fig. 4A).

One reason that NMNAT2 loss affects axonal transport in distal but not proximal axons may be that its homolog NMNAT1, which is expressed in the neuronal nucleus, is sufficient to maintain NAD redox potential in the soma and proximal axons [14, 80]. Thus, we hypothesized that NMNAT2 is only critical for maintaining NAD redox potential in distal axons, where it provides the ATP required for fast axonal transport. So, to measure NAD redox potential in sub-axonal regions, we used a genetically encoded sensor, SoNar [44], that detects cytosolic NAD redox potential with a reliable signal-to-noise ratio and high spatial resolution. Our imaging studies found that NAD redox potential was significantly reduced in distal axons but not in the soma or proximal axons of DIV8 KO neurons compared to controls (Fig. 4B-C). These

data confirm the requirement of NMNAT2 in distal axons to maintain NAD redox potential. In addition, the data suggest that NMNAT2 contributes to ~ 50% of the overall NAD^+ and NADH levels in cortical neurons.

NMNAT2 is critical for glycolysis on synaptic vesicles

Fast axonal transport of vesicular cargo is fueled by on-board glycolysis through vesicle-associated glycolytic enzymes that generate ATP to support motor protein movement [32, 81]. Considering the transport deficits and the reduced NAD^+/NADH redox potential in the distal axons of NMNAT2 KO neurons, we hypothesized that NMNAT2 supports fast axonal transport by facilitating local glycolysis. To measure ATP near fast-moving vesicular cargos, we transfected the genetically encoded presynaptic ATP sensor (Syn-ATP) in control and NMNAT2 KO neurons and measured ATP levels in distal axons at DIV 8 with live imaging (Fig. 5). This sensor is targeted to synaptophysin, one of the well-known fast vesicular cargos. Syn-ATP comprises an optimized luciferase to detect ATP by luminescence and an mCherry fluorescent protein as an internal control for sensor expression level [33] (Fig. 5B). The luminescence to fluorescence ratio (L/F) measured from Syn-ATP is proportional to ATP levels near synaptic vesicles (sv-ATP) [33]. As the Syn-ATP sensor is pH sensitive [33], all the measurements were pH-corrected (Fig. 5-S1A-C).

NMNAT2 KO neurons exhibited a modest but significant decrease in sv-ATP compared to control neurons (Fig. 5C,D). sv-ATP can come from local glycolysis and/or mitochondrial ATP synthesis [82]. To check if it was contributed by glycolysis, we applied oligomycin, an F_1-F_0 ATP synthase inhibitor that blocks mitochondrial ATP production (Fig. 5A,B). Previous findings show that glycolytic ATP production is the primary ATP source for fast-transporting cargos [32, 81]. However, we found no significant reduction in sv-ATP levels ($p = 0.3621$) in control distal axons upon oligomycin treatment (Fig. 5C,D). However, in KO distal axons, oligomycin treatment significantly and strongly reduced sv-ATP levels (Fig. 5C,D), suggesting that in the absence of NMNAT2, mitochondria provide ATP in distal axons. These data strongly indicate that NMNAT2 is required to drive glycolysis on synaptic vesicles.

To test if the reduced sv-ATP in NMNAT2 KO axons is caused by NAD^+ deficiency, neuronal cultures were supplemented with 1 mM NAD^+ from DIV5 to DIV8 (Fig. 5A). Isotope labeling studies show that primary neuronal cultures can take up exogenous NAD^+ [83, 84]. Here we found that NAD^+ supplementation increased intracellular NAD^+ levels transiently in neuronal cultures (Fig. 5-S2) and thus we refreshed NAD^+ daily. NAD^+ supplementation restored sv-ATP levels in KO distal axons to control levels in both basal and oligomycin treated conditions (Fig. 5C-D). These data suggest that NMNAT2 synthesizes the NAD^+ required to drive glycolysis on synaptic vesicles.

NAD supplementation restores APP transport via glycolysis in the absence of NMNAT2

Next, we determined whether NAD^+ supplementation can restore fast axonal transport in NMNAT2 KO distal axons. Compared to vehicle treatment, NAD^+ supplementation significantly decreased the percentage of stationary/dynamic pause events, increased the percentage of anterograde and retrograde events, and restored anterograde and retrograde velocities of APP transport (Fig. 6A-C). On the other hand, NAD^+ supplementation of control neurons had minimal impact on APP axonal transport (Fig. 6A-C) and NAD^+ abundance (Fig. 5-S2).

We then tested whether glycolysis is required for NAD^+ rescue of APP transport. We acutely suppressed glycolysis by transferring the neurons to a glucose-free medium containing the hexokinase inhibitor, 2-deoxyglucose (2DG), while adding methyl-pyruvate (Methyl-pyr) as an alternative substrate to support TCA cycle and OXPHO in mitochondria (Fig. 6D,E). In parallel, we tested if mitochondrial ATP production is required for NAD^+ rescue of axonal transport in NMNAT2 KO neurons by blocking OXPHO in the presence of glucose (Fig. 6D,E). Glycolysis inhibition significantly impaired APP transport in control axons, as revealed by a significant increase in stationary/dynamic pause events and decrease in transport velocity (Fig. 6F,G). In fact, the substantially reduced mobile APP-tagged vesicles in glycolysis-inhibited cultures made it challenging to image sufficient vesicles for velocity measurements. In contrast, OXPHO inhibition had a relatively mild impact on APP transport in control axons, including a moderate reduction in anterograde velocity and a minor but significant increase in the percentage of retrograde events. In KO axons, glycolysis inhibition abolished the rescue of APP transport provided by exogenous NAD^+ and significantly reduced the number of transport events and movement velocities (Fig. 6F,G).

OXPHO inhibition also perturbed NAD^+-mediated rescue of KO neurons, although not as robustly as did glycolysis inhibition, as shown by the increased percentage of stationary/dynamic pause events and decreased percentage of anterograde events (Fig. 6F). However, the transport velocities in both directions were unaffected (Fig. 6G). Additionally, we assessed APP accumulation by immunostaining and found that NAD^+ supplementation from DIV8 to 14 significantly reduces APP accumulation in KO neurons. Furthermore, 48 hours of glycolysis inhibition together with methyl-pyruvate supplementation abolished this rescue (Fig. 6-S1A-C). These data demonstrate that NAD^+-mediated rescue of APP axonal transport in NMNAT2 KO neurons depends mainly on glycolysis with a modest contribution from mitochondrial OXPHO.

SARM1 depletion sustains APP transport and prevents axon degeneration in the absence of NMNAT2

Sterile alpha and TIR motif-containing protein 1 (SARM1) is a recently discovered NAD(P) glycol-hydrolase highly expressed in neurons [85, 86]. SARM1 senses the rise in nicotinamide mononucleotide (NMN)-to-NAD^+ ratio caused by loss of NMNAT2 and responds by activating its NAD^+ hydrolase domain [87, 88]. SARM1 deletion in NMNAT2 KO mice prevents perinatal lethality, preserves healthy axons and synapses in the peripheral nervous system, and maintains motor function throughout adulthood [89, 90].

We, therefore, examined if SARM1 reduction could reverse axon phenotypes in NMNAT2 cKO brains. To this end, we crossed NMNAT2 cKO mice to SARM1 KO (S^{null}/S^{null}) mice to generate NMNAT2 cKO missing one copy of SARM1 (NMNAT2 cKO; $S^{null}/+$), which we backcrossed to SARM1 KO mice to obtain NMNAT2 cKO missing both copies of SARM1 (NMNAT2 cKO; S^{null}/S^{null}). NMNAT2 cKO; $S^{null}/+$ and NMNAT2 cKO; S^{null}/S^{null} mice survived similarly to their littermate controls, in contrast to NMNAT2 cKO mice (data not shown). Normal brain morphology was observed in NMNAT2 cKO; S^{null}/S^{null} mice (Fig. 7A). In contrast to NMNAT2 cKO; S^{null}/S^{null} mice and control mice, NMNAT2 cKO; $S^{null}/+$ mice still exhibited reduced body weights (Fig. 7-S1B). Gross examination of their brains found aberrant anatomy similar to NMNAT2 cKO brains (Fig. 7A), including atrophied hippocampi, enlarged ventricles, and thinned primary somatosensory cortex (Fig. 7B) and corpus callosum (Fig. 7C,D). APP accumulation was found in the corpus callosum, fimbria, and striatum in NMNAT2 cKO; $S^{null}/+$ but not in NMNAT2 cKO; S^{null}/S^{null} brains (Fig. 7E,F). APP accumulation was detectable at P5 in NMNAT2 cKO; $S^{null}/+$ but not NMNAT2 cKO; S^{null}/S^{null} brains, suggesting APP transport was already normalized by the complete absence of SARM1 at P5 (Fig. 7-S2). Taken together, these findings show that complete SARM1 loss prevents the impact of NMNAT2 loss in cortical axons.

Next, we examined whether SARM1 loss protects NMNAT2 KO neurons from axonal degeneration by preventing axonal transport deficit. We used anti-sense oligonucleotides targeting *sarm1* mRNA (SARM1-ASO) to knockdown SARM1 expression at desired time points and a scrambled anti-sense oligonucleotide as the non-targeting control (ctrl-ASO). We evaluated the SARM1 knockdown efficacy of two SARM1-ASOs and one ctrl-ASO using qPCR and western blotting. ASO33, one of the two SARM1-ASOs, significantly decreased SARM1 protein abundance 4–7 days following ASO treatment (Fig. 8-S1). This ASO was therefore used for the rest of the experiments and referred to as SARM1-ASO. To test the impact of SARM1 knockdown on axonal transport, we added ASOs from DIV1 and DIV5 on and examined the impact at DIV8. SARM1-ASO application starting at DIV1 significantly reduced SARM1 abundance by ~ 70% and prevented APP transport deficits in NMNAT2 KO axons at DIV8 (Fig. 8A1-4). In contrast, SARM1-ASO treatment starting at DIV5 only reduced SARM1 abundance by ~ 50% and failed to rescue axonal transport (Fig. 8B1-4). Surprisingly, by DIV12, APP transport was completely rescued in the distal axons of these neurons (Fig. 8C1-4), despite the impairment at DIV8. Consistent with axonal transport analysis, APP accumulation at DIV14 was rescued by SARM1-ASO treatment starting from DIV1 or DIV5 in NMNAT2 KO neurons (Fig. 8-S2). Furthermore, the axon degeneration phenotype revealed by TUJ1 aggregates at DIV14 in ctrl-ASO-treated NMNAT2 KO axons was also reduced by SARM1-ASO treatment. Thus, blocking NAD^+ degradation by SARM1 depletion protects axons during NMNAT2 loss *in vivo* and *in vitro*.

Discussion

NMNAT2 has been identified as an AD target and an axonal maintenance factor. Here we provide the first *in vivo* evidence that NMNAT2 is critical for the health of long-range cortical glutamatergic axons in mice. We show that NMNAT2 loss impairs glycolysis, disrupts fast axonal transport, and results in APP

accumulation. NAD^+ supplementation or reducing the levels of SARM1, an NAD^+ hydrolase, effectively restores fast axonal transport and prevents the neurodegeneration commonly observed in NMNAT2 cKO axons both *in vitro* and *in vivo*. In summary, our present study suggests that NMNAT2 protects cortical neurons from axonal degeneration by ensuring that the energetic demands of distal axons are met. Our data also suggest glucose hypometabolism in long-range axons is likely a major cause of axonopathy during NDAs. Therefore, therapies in preventing NMNAT2 or NAD loss during aging or NDAs should maintain axonal energetics and axonal health.

NMNAT2 contributes to fast axonal transport by maintaining the local NAD redox potential for efficient vesicular glycolysis

In this study, we show that NMNAT2 is required for maintaining vesicular glycolytic activity (Fig. 5) and the fast axonal transport of APP and SNAP25-containing vesicular cargos (Fig. 3) in distal axons of cortical neurons. This role in vesicular cargo transport is consistent with earlier observations. For instance, NMNAT2 is enriched in the synaptic vesicle and membrane but not in mitochondrial fractions of cortical neurons [91]. In addition, the palmitoylation of NMNAT2 enables it to associate with the membrane of Golgi-derived, fast-moving vesicular cargos [25]. Our time-lapse imaging confirms that NMNAT2's dynamic antero- and retrograde movement and transport velocities in axons are similar to fast-transported cargos like APP- and SNAP25-containing vesicles (Fig. 3-S1).

Glycolysis is the primary ATP source for fast axonal transport and is generated by a vesicular glycolytic complex [32, 81]. It has been estimated that one kinesin requires ~ 187.5 ATP molecules/s to move at ~ 1.5 μm/s [36], the average anterograde velocity of APP. Thus, ~ 188 NAD^+ molecules of NAD^+ are needed to drive ~ 94 glycolytic reactions per second near individual vesicular cargos to generate the ATP consumed by one kinesin. Data from our SoNar NAD^+/NADH radiometric imaging studies show that NMNAT2 is essential in maintaining the NAD redox potential in distal axons. Based on *in vitro* biochemical studies, one NMNAT2 synthesizes ~ 0.6 NAD^+ per second [91]. Knowing that lactate dehydrogenases (LDH) can catalyze NADH recycling back to NAD^+, we hypothesize that NMNAT2 coordinates with LDH to maintain NAD redox potential for glycolytic ATP production. Furthermore, our data suggest that NMNAT2's NAD^+ synthesizing activity and proximity to the vesicular glycolytic complex ensure sufficient ATP for motor protein operation in fast axonal transport.

Intriguingly, before DIV8, NMNAT2 seems to be dispensable for axonal extension and axonal transport, which also requires glycolytic ATP supply [92]. We speculate that other mechanisms, such as the newly discovered Wnk kinases [93], exist in the early developmental stage to ensure NAD homeostatic balance in the absence of NMNAT2, allowing a sufficient level of glycolytic flux to fuel cargo transport, cytoskeleton dynamics, and axon outgrowth. However, by DIV8 *in vitro* and P16/21 *in vivo*, NMNAT2 becomes the mandatory source of NAD^+, but only in distal axonal segments. In proximal axons, NMNAT2 is dispensable for NAD redox potential maintenance and fast axonal transport. Given that the NAD^+ pool between the nucleus and soma is interchangeable [45], proximal axons could potentially receive sufficient

NAD^+ generated by nuclear NMNAT1 due to their proximity to soma and thus maintain an adequate NAD redox potential to drive proximal axonal transport despite the absence of NMNAT2. Alternatively, OXPHO from somatic mitochondria could fuel axonal transport in proximal axons of NMNAT2 KO neurons. Electron microscopy studies of cortical layers 2/3 of the primary visual cortex show that the proximal axons within 100 μm from somata of pyramidal neurons tend to have higher mitochondrial coverage and volume than distal axons [94]. Mitochondria tend to be smaller, and less mobile in distal axons [94–97]. As mitochondria are smaller and less mobile in distal axons [94–97], we hypothesize that higher coverage of mitochondria in proximal axons compensates for the glycolysis deficits in NMNAT2 KO neurons to fuel fast axonal transport.

Previous studies indicate that BDNF axonal transport is mainly fueled by glycolysis, and unaffected by ablating mitochondrial OXPHO [32]. Our data is largely consistent with this finding on glycolysis-dependent fast axonal transport. However, upon OXPHO inhibition, we observed a mild but significant increase in the numbers of APP cargos undergoing retrograde transport, with a concomitant decrease in anterograde velocity. Using *Drosophila* neurodegenerative models, it has been shown that mitochondrial dysfunction stimulates a retrograde signaling response [98]. APP is partially localized on the endo-lysosomal vesicles involved in retrograde transport [99, 100]. Thus, the increase in retrograde APP cargo upon mitochondrial inhibition can reflect enhanced retrograde signaling.

Accumulation of APP, a pathological hallmark of defective axonal transport [67, 101], was found in regions enriched with long-range axons of NMNAT2 cKO brains already at P5, preceding the obvious axonal loss. No APP accumulation was observed in the cortex, where proximal or short axonal arbors are enriched. Using cultured neurons, we demonstrated that the fast axonal transport of APP and SNAP25 is severely impaired in distal axonal segments of NMNAT2 KO neurons. These *in vitro* observations of specific axonal transport deficits in distal axons of NMNAT2 KO cortical neurons offer a mechanistic explanation for the APP accumulation in long-range axons observed in cKO brains. Together, our study provides strong evidence that NMNAT2 is required for fast axonal transport in distal axons of cortical glutamatergic neurons.

Cumulative evidence suggests that neuronal subtypes with long and complex axonal arbors are particularly vulnerable to external insults [102, 103]. As NMNAT2 cKO brains reach the age of P16-P21, not only does APP accumulation drastically increase, but severe axon degeneration occurs, along with a reduction in cortical thickness, hippocampal atrophy, ventricle enlargement, and motor behavioral deficits, recapitulating major hallmarks of neurodegeneration. These findings support the hypothesis that defective axonal transport drives axonopathy in the pre-symptomatic phase of neurodegeneration [54, 104], which may serve as the focal basis for the gradual development and spread of secondary neuronal damage [105, 106]. However, we do not exclude a possible role of NMNAT2 in maintaining neuronal health in the dendritic and somatic compartments [107, 108], whose dysfunction could also contribute to neurodegenerative phenotypes in NMNAT2 cKO brains.

Mitochondrial OXPHO as a mediator of axonal degeneration in NMNAT2 KO cortical neurons

Our sv-ATP imaging studies show significantly reduced ATP levels in NMNAT2 KO distal axons when mitochondrial function is blocked (Fig. 5). By contrast, in control cortical axons, mitochondrial inhibition has a negligible impact on sv-ATP levels. These observations suggest that NMNAT2 loss results in a shift towards mitochondrial OXPHO to maintain sv-ATP levels, however, not enough to fuel fast axonal transport. The literature suggests two mechanisms that could mediate this shift in CNS neurons: (1) Ca^{2+} signaling-dependent regulation of mitochondrial calcium uniporters and the malate-aspartate shuttle [109–111]; (2) The O-GlcNAcylation-dependent post-translational modification of the mitochondrial proteome and mitochondrial motility [112, 113]. It remains unclear why this metabolic shift fails to protect NMNAT2 KO neurons from axonal degeneration: at DIV14, NMNAT2 KO axons exhibit prominent blebbing, a degenerative-like phenotype (Fig. 8-S2B). It has been suggested that the cumulative oxidative stress and depletion of TCA cycle substrates from hyperactive mitochondrial OXPHO could be detrimental to neuronal survival in PD and AD animal models [114–116]. This observation raises the possibility that excessive mitochondrial activity, compensating for defective glycolysis in NMNAT2 KO axons, contributes to axon degeneration.

We suspect SARM1 depletion not only mitigates the harmful impact of excessive OXPHO, but also sustains OXPHO by preventing mitochondrial NAD^+ pool decline, thus offering excellent rescue in NMNAT2 KO neurons. Endogenous SARM1 widely distributes along neurites as small puncta [47, 117]. Upon mitochondrial stress or overexpression, SARM1 localizes onto the mitochondrial outer membrane and interacts with mitophagy machinery [85, 86, 118, 119]. SARM1 is a NAD^+ consuming enzyme and its NAD^+ hydrolase activity can be activated by the rise of NMN to NAD^+ ratio [87], or by JNK-mediated phosphorylation [120]. It has been shown that SARM1 in activated state drastically consumes NAD^+ and impairs mitochondrial OXPHO [120]. In an axotomy model, the mitochondrial motility is preserved when SARM1 is genetically deleted [121]. In the Charcot-Marie-Tooth neuropathy model with mitochondrial abnormality, SARM1 deletion preserved mitochondrial morphology and motility, and protected axons and synapses from degeneration [122]. Here we find that SARM1 loss prevents several phenotypes caused by NMNAT2 loss, including the impaired fast axonal transport and axonal morphology. Currently, it is still unknown whether SARM1 removal in NMNAT2 KO axons prevents the oxidative stress caused by mitochondria hyperactivity. Further investigations into the impacts of SARM1 deletion from NMNAT2 KO axons on mitochondrial metabolic capacity, dynamics, NAD^+-NADH shuttling between mitochondrial matrix and cytoplasm, and mitochondrial quality control are needed.

NMNAT2 and vesicular glycolysis as potential targets to protect white matter in neurodegenerative diseases

Positron emission tomography (FDG-PET) studies have shown that glucose metabolism changes during aging/NDAs in specific brain regions [123–128]. In particular, glucose hypometabolism is often detected

in AD-susceptible brain regions and strongly predicts the incidence of mild-cognitive impairment (MCI) in later life [129–133]. The majority of AD-susceptible regions for cognitive decline identified are located in the default mode network (DMN), the topological central hub of the brain connectome [134–136]. Anatomically, these hub areas are densely inter-connected by long-range axonal tracts [137], that often show pathological changes since early-stage disease [138]. Metabolically, these connectome hubs express higher levels of glycolysis genes compared to the non-hub areas [139], and exhibit reduced aerobic glycolysis upon normal aging and AD [140, 141], which positively correlates with white matter deterioration [142]. Notably, glucose hypometabolism is observed directly in white matter tracts of AD brains [4].

We show that NMNAT2 is critical for vesicular glycolysis to fuel axonal transport in distal axons. Previously, we have demonstrated that NMNAT2 levels are significantly reduced in the prefrontal cortex of AD brains [21], one of the DMN hubs. Our biochemical assays reveal a ~ 50% reduction of NAD^+ and NADH levels in NMNAT2 KO neurons (Fig. 4A), indicating that NMNAT2 is a major NAD^+ and NADH provider in cortical neurons. Synthesizing these observations, we hypothesize that reduced NMNAT2 in AD brains contributes, at least in part, to the reduction in glucose metabolism observed in AD white matter.

NMNAT2 reduction has also been observed in PD and HD brains [21–23]. PD patients show hypometabolism in the premotor and parieto-occipital cortex that correlates with motor dysfunction [128], while HD patients show progressive glucose hypometabolism in the frontal lobe, temporal lobe, and striatum, accompanied by white matter volume reduction [125]. Supplementing NAD^+ and its precursors remarkably ameliorates degenerative phenotypes in transgenic AD and ALS mouse models [143–145]. Similarly, increasing NMNAT2 expression broadly provides neuroprotection across mouse models of tauopathy [21, 146], familiar AD [147], and glaucoma [148]. Coincidently, upregulating glycolysis exerts neuroprotective effect in PD synucleinopathy and ALS models [149, 150]. Our study highlights a novel role of NMNAT2 in supporting glycolysis in long-range projecting axons of cortical glutamatergic neurons. Extrapolating from our findings, NMNAT2 could serve as a putative therapeutic target to boost neuronal glycolysis in order to antagonize the structural connectome breakdown occurring in many neurodegenerative disorders.

Abbreviations

2DG
2-deoxyglucose
AD
Alzheimer's disease
ALS
Amyotrophic lateral sclerosis
APP
Amyloid precursor protein

ASO
Antisense oligonucleotide
cKO
Conditional knockout
CP
Cortical plate
Cyto-pHluorin
Cytoplasmic pHluorin
DIV
Days *in vitro*
DMN
Default mode network
ELF1alpha
Elongation factor 1 alpha
FDG-PET
Fludeoxyglucose positron emission tomography
HET
Heterozygous
JNK
c-Jun N-terminal kinase
L/F
Luminescence to fluorescence ratio
LDH
Lactate dehydrogenase
LGE
Lateral ganglionic eminence
MBP
Myelin basic protein
MCI
Mild-cognitive impairment
Methyl-pyr
Methyl-pyruvate
MGE
Medial ganglionic eminence
MOI
Multiplicity of infection
NAD
Nicotinamide adenine dinucleotide
NDA
Neurodegenerative disorders of aging

NF-M
Medium-size neurofilament
NMNAT2
Nicotinamide mononucleotide adenylyl transferase 2
Oligo
Oligomycin
OXPHO
Oxidative phosphorylation
PDL
Poly-D-lysine
PFA
Paraformaldehyde
ROI
Region of interest
SARM1
Sterile alpha and TIR motif-containing protein 1
SNAP25
Synaptosome associated protein 25
sv-ATP
ATP levels near synaptic vesicles
TCA
Tricarboxylic acid
TUJ1
βIII-tubulin
WT
Wildtype

Declarations

Acknowledgments

We thank the following: Dr. Yuyu Song for helpful discussions; Light Microscopy Imaging Center and Dr. Jim Powers in Indiana University Bloomington for live cell imaging (supported by NIH1S10OD024988); Gene vector core directed by Dr. Kazu Oka at Baylor College of Medicine for lentivirus production; Dr. Yi Yang for providing SoNar sensor; Drs. Feng Guo, István Katona for sharing equipment; Dr. Ken Mackie for pCAG-mCherry plasmid and reading the manuscript; László Barna, John Reinhart, Scott Barton, Theo Knowles, Caliel D. Hines and Kelsie Godsey for technical assistance; Dr. JangDong Seo in Indiana statistical consulting center for statistical assistance.

Funding

This work was supported by National Institutes of Health grant NINDS NS086794 (H.C.L), NIGMS R35GM119557 (J.M.T.), Max Planck Society (V.R.), Indiana Clinical and Translational Sciences Institute funded by National Institutes of Health UL1TR002529 (Indiana University Research Community)

Author contributions

Conceptualization: SY, HCL., VR, JMT, JYH.

Experimentation/Investigation: SY, ZXN, JL, AE

Data acquisition: SY, ZXN, JL, AE

Data curation: SY, VR, ZXN, AE

Methodology: VR, JYH, PJN, KL, JG, MPC

Writing: SY, ZXN, AE, VR, HCL

Funding acquisition: HCL

Resource: HCL, VR

Supervision: HCL, VR

Availability of data and materials

Supplementary Material, Tables and material will be provided upon request.

Ethics approval and consent to participate

Not applicable

Consent for publication

Not applicable

Competing interests:

All authors declare they have no competing interests.

Data and materials availability: All data are available in the main text or the supplementary materials.

Author Details

The Linda and Jack Gill Center for Biomolecular Sciences and Department of Psychological and Brain Sciences, Program in Neuroscience, Indiana University, Bloomington, IN 47405

Sen Yang, Zhen-Xian Niou, Andrea Enriquez, Jui-Yen Huang, Jacob LaMar, & Hui-Chen Lu

Department of Biology, Indiana University, Bloomington, IN 47405

Jason M. Tennessen

Max Planck Florida Institute for Neuroscience, Jupiter, FL, USA

Jacob LaMar, Vidhya Rangaraju

Department of Clinical Neuroscience, Cambridge University, Cambridge, United Kingdom.

Jonathan Gilley, Michael P. Coleman

Neuroscience Drug Discovery, Ionis Pharmaceuticals, Inc., 2855 Gazelle Court, Carlsbad, CA 92010, USA.

Karen Ling, Paymaan Jafar-Nejad

***Corresponding author Hui-Chen Lu (hclu@indiana.edu)**

References

1. Harris JJ, Attwell D. The energetics of CNS white matter. J Neurosci. 2012;32:356–71.
2. Yellen G. Fueling thought: Management of glycolysis and oxidative phosphorylation in neuronal metabolism. J Cell Biol. 2018;217:2235–46.
3. Shokhirev MN, Johnson AA. An integrative machine-learning meta-analysis of high-throughput omics data identifies age-specific hallmarks of Alzheimer's disease. Ageing Res Rev. 2022;81:101721.
4. Roy M, Rheault F, Croteau E, Castellano CA, Fortier M, St-Pierre V, Houde JC, Turcotte EE, Bocti C, Fulop T, et al. Fascicle- and Glucose-Specific Deterioration in White Matter Energy Supply in Alzheimer's Disease. J Alzheimers Dis. 2020;76:863–81.
5. Wang M, Liu K, Pan J, Li J, Sun P, Zhang Y, Li L, Guo W, Xin Q, Zhao Z, et al. Brain-wide projection reconstruction of single functionally defined neurons. Nat Commun. 2022;13:1531.
6. Winnubst J, Bas E, Ferreira TA, Wu Z, Economo MN, Edson P, Arthur BJ, Bruns C, Rokicki K, Schauder D, et al. Reconstruction of 1,000 Projection Neurons Reveals New Cell Types and Organization of Long-Range Connectivity in the Mouse Brain. Cell. 2019;179:268–281e213.
7. Peng H, Xie P, Liu L, Kuang X, Wang Y, Qu L, Gong H, Jiang S, Li A, Ruan Z, et al. Morphological diversity of single neurons in molecularly defined cell types. Nature. 2021;598:174–81.
8. Coleman MP. The challenges of axon survival: introduction to the special issue on axonal degeneration. Exp Neurol. 2013;246:1–5.
9. Zhang J, Long B, Li A, Sun Q, Tian J, Luo T, Ding Z, Gong H, Li X. Whole-Brain Three-Dimensional Profiling Reveals Brain Region Specific Axon Vulnerability in 5xFAD Mouse Model. Front Neuroanat. 2020;14:608177.

10. Stokin GB, Lillo C, Falzone TL, Brusch RG, Rockenstein E, Mount SL, Raman R, Davies P, Masliah E, Williams DS. Axonopathy and transport deficits early in the pathogenesis of Alzheimer's disease. Science. 2005;307:1282–8.
11. Fischer LR, Culver DG, Tennant P, Davis AA, Wang M, Castellano-Sanchez A, Khan J, Polak MA, Glass JD. Amyotrophic lateral sclerosis is a distal axonopathy: evidence in mice and man. Exp Neurol. 2004;185:232–40.
12. Xiao AW, He J, Wang Q, Luo Y, Sun Y, Zhou YP, Guan Y, Lucassen PJ, Dai JP. The origin and development of plaques and phosphorylated tau are associated with axonopathy in Alzheimer's disease. Neurosci Bull. 2011;27:287–99.
13. Jones DP, Sies H. The Redox Code. Antioxid Redox Signal. 2015;23:734–46.
14. Berger F, Lau C, Dahlmann M, Ziegler M. Subcellular compartmentation and differential catalytic properties of the three human nicotinamide mononucleotide adenylyltransferase isoforms. J Biol Chem. 2005;280:36334–41.
15. Raffaelli N, Sorci L, Amici A, Emanuelli M, Mazzola F, Magni G. Identification of a novel human nicotinamide mononucleotide adenylyltransferase. Biochem Biophys Res Commun. 2002;297:835–40.
16. Yan T, Feng Y, Zheng J, Ge X, Zhang Y, Wu D, Zhao J, Zhai Q. Nmnat2 delays axon degeneration in superior cervical ganglia dependent on its NAD synthesis activity. Neurochem Int. 2010;56:101–6.
17. Coleman MP, Hoke A. Programmed axon degeneration: from mouse to mechanism to medicine. Nat Rev Neurosci. 2020;21:183–96.
18. Gerdts J, Summers DW, Milbrandt J, DiAntonio A. Axon Self-Destruction: New Links among SARM1, MAPKs, and NAD + Metabolism. Neuron. 2016;89:449–60.
19. Simon DJ, Watkins TA. Therapeutic opportunities and pitfalls in the treatment of axon degeneration. Curr Opin Neurol. 2018;31:693–701.
20. Gilley J, Coleman MP. Endogenous Nmnat2 is an essential survival factor for maintenance of healthy axons. PLoS Biol. 2010;8:e1000300.
21. Ali YO, Allen HM, Yu L, Li-Kroeger D, Bakhshizadehmahmoudi D, Hatcher A, McCabe C, Xu J, Bjorklund N, Taglialatela G, et al. NMNAT2:HSP90 Complex Mediates Proteostasis in Proteinopathies. PLoS Biol. 2016;14:e1002472.
22. Bennett JP, Keeney PM. RNA-Sequencing Reveals Similarities and Differences in Gene Expression in Vulnerable Brain Tissues of Alzheimer's and Parkinson's Diseases. J Alzheimers Dis Rep. 2018;2:129–37.
23. Ali YO, Li-Kroeger D, Bellen HJ, Zhai RG, Lu HC. NMNATs, evolutionarily conserved neuronal maintenance factors. Trends Neurosci. 2013;36:632–40.
24. Brazill JM, Li C, Zhu Y, Zhai RG. NMNAT: It's an NAD(+) synthase… It's a chaperone… It's a neuroprotector. Curr Opin Genet Dev. 2017;44:156–62.

25. Milde S, Gilley J, Coleman MP. Subcellular localization determines the stability and axon protective capacity of axon survival factor Nmnat2. PLoS Biol. 2013;11:e1001539.
26. Hung CO, Coleman MP. KIF1A mediates axonal transport of BACE1 and identification of independently moving cargoes in living SCG neurons. Traffic. 2016;17:1155–67.
27. Guedes-Dias P, Holzbaur ELF. Axonal transport: Driving synaptic function. Science 2019, 366.
28. Sleigh JN, Rossor AM, Fellows AD, Tosolini AP, Schiavo G. Axonal transport and neurological disease. Nat Rev Neurol. 2019;15:691–703.
29. Pacelli C, Giguere N, Bourque MJ, Levesque M, Slack RS, Trudeau LE. Elevated Mitochondrial Bioenergetics and Axonal Arborization Size Are Key Contributors to the Vulnerability of Dopamine Neurons. Curr Biol. 2015;25:2349–60.
30. Gallo G. The bioenergetics of neuronal morphogenesis and regeneration: Frontiers beyond the mitochondrion. Dev Neurobiol. 2020;80:263–76.
31. Chamberlain KA, Sheng ZH. Mechanisms for the maintenance and regulation of axonal energy supply. J Neurosci Res. 2019;97:897–913.
32. Zala D, Hinckelmann MV, Yu H, Lyra da Cunha MM, Liot G, Cordelieres FP, Marco S, Saudou F. Vesicular glycolysis provides on-board energy for fast axonal transport. Cell. 2013;152:479–91.
33. Rangaraju V, Calloway N, Ryan TA. Activity-driven local ATP synthesis is required for synaptic function. Cell. 2014;156:825–35.
34. Faitg J, Lacefield C, Davey T, White K, Laws R, Kosmidis S, Reeve AK, Kandel ER, Vincent AE, Picard M. 3D neuronal mitochondrial morphology in axons, dendrites, and somata of the aging mouse hippocampus. Cell Rep. 2021;36:109509.
35. Santuy A, Turegano-Lopez M, Rodriguez JR, Alonso-Nanclares L, DeFelipe J, Merchan-Perez A. A Quantitative Study on the Distribution of Mitochondria in the Neuropil of the Juvenile Rat Somatosensory Cortex. Cereb Cortex. 2018;28:3673–84.
36. Schnitzer MJ, Block SM. Kinesin hydrolyses one ATP per 8-nm step. Nature. 1997;388:386–90.
37. Gilley J, Adalbert R, Yu G, Coleman MP. Rescue of peripheral and CNS axon defects in mice lacking NMNAT2. J Neurosci. 2013;33:13410–24.
38. Goebbels S, Bormuth I, Bode U, Hermanson O, Schwab MH, Nave KA. Genetic targeting of principal neurons in neocortex and hippocampus of NEX-Cre mice. Genesis. 2006;44:611–21.
39. Hicks AN, Lorenzetti D, Gilley J, Lu B, Andersson KE, Miligan C, Overbeek PA, Oppenheim R, Bishop CE. Nicotinamide mononucleotide adenylyltransferase 2 (Nmnat2) regulates axon integrity in the mouse embryo. PLoS ONE. 2012;7:e47869.
40. Kim Y, Zhou P, Qian L, Chuang JZ, Lee J, Li C, Iadecola C, Nathan C, Ding A. MyD88-5 links mitochondria, microtubules, and JNK3 in neurons and regulates neuronal survival. J Exp Med. 2007;204:2063–74.
41. Currinn H, Guscott B, Balklava Z, Rothnie A, Wassmer T. APP controls the formation of PI(3,5)P(2) vesicles through its binding of the PIKfyve complex. Cell Mol Life Sci. 2016;73:393–408.

42. Galiano MR, Jha S, Ho TS, Zhang C, Ogawa Y, Chang KJ, Stankewich MC, Mohler PJ, Rasband MN. A distal axonal cytoskeleton forms an intra-axonal boundary that controls axon initial segment assembly. Cell. 2012;149:1125–39.
43. Kitay BM, McCormack R, Wang Y, Tsoulfas P, Zhai RG. Mislocalization of neuronal mitochondria reveals regulation of Wallerian degeneration and NMNAT/WLD(S)-mediated axon protection independent of axonal mitochondria. Hum Mol Genet. 2013;22:1601–14.
44. Zhao Y, Hu Q, Cheng F, Su N, Wang A, Zou Y, Hu H, Chen X, Zhou HM, Huang X, et al. SoNar, a Highly Responsive NAD+/NADH Sensor, Allows High-Throughput Metabolic Screening of Anti-tumor Agents. Cell Metab. 2015;21:777–89.
45. Cambronne XA, Stewart ML, Kim D, Jones-Brunette AM, Morgan RK, Farrens DL, Cohen MS, Goodman RH. Biosensor reveals multiple sources for mitochondrial NAD(+). Science. 2016;352:1474–7.
46. Fletcher TL, Cameron P, De Camilli P, Banker G. The distribution of synapsin I and synaptophysin in hippocampal neurons developing in culture. J Neurosci. 1991;11:1617–26.
47. Chen CY, Lin CW, Chang CY, Jiang ST, Hsueh YP. Sarm1, a negative regulator of innate immunity, interacts with syndecan-2 and regulates neuronal morphology. J Cell Biol. 2011;193:769–84.
48. Clements RT, Fuller LE, Kraemer KR, Radomski SA, Hunter-Chang S, Hall WC, Kalantar AA, Kraemer BR. Quantification of Neurite Degeneration with Enhanced Accuracy and Efficiency in an In Vitro Model of Parkinson's Disease. eNeuro 2022, 9.
49. Chou AH, Yeh TH, Ouyang P, Chen YL, Chen SY, Wang HL. Polyglutamine-expanded ataxin-3 causes cerebellar dysfunction of SCA3 transgenic mice by inducing transcriptional dysregulation. Neurobiol Dis. 2008;31:89–101.
50. Lieu CA, Chinta SJ, Rane A, Andersen JK. Age-related behavioral phenotype of an astrocytic monoamine oxidase-B transgenic mouse model of Parkinson's disease. PLoS ONE. 2013;8:e54200.
51. Wang X, Zhang Q, Bao R, Zhang N, Wang Y, Polo-Parada L, Tarim A, Alemifar A, Han X, Wilkins HM, et al. Deletion of Nampt in Projection Neurons of Adult Mice Leads to Motor Dysfunction, Neurodegeneration, and Death. Cell Rep. 2017;20:2184–200.
52. Wang CL, Zhang L, Zhou Y, Zhou J, Yang XJ, Duan SM, Xiong ZQ, Ding YQ. Activity-dependent development of callosal projections in the somatosensory cortex. J Neurosci. 2007;27:11334–42.
53. Fame RM, MacDonald JL, Macklis JD. Development, specification, and diversity of callosal projection neurons. Trends Neurosci. 2011;34:41–50.
54. Stokin GB, Lillo C, Falzone TL, Brusch RG, Rockenstein E, Mount SL, Raman R, Davies P, Masliah E, Williams DS, Goldstein LS. Axonopathy and transport deficits early in the pathogenesis of Alzheimer's disease. Science. 2005;307:1282–8.
55. Fu MM, Holzbaur EL. JIP1 regulates the directionality of APP axonal transport by coordinating kinesin and dynein motors. J Cell Biol. 2013;202:495–508.
56. Gunawardena S, Goldstein LS. Disruption of axonal transport and neuronal viability by amyloid precursor protein mutations in Drosophila. Neuron. 2001;32:389–401.

57. Kamal A, Stokin GB, Yang Z, Xia CH, Goldstein LS. Axonal transport of amyloid precursor protein is mediated by direct binding to the kinesin light chain subunit of kinesin-I. Neuron. 2000;28:449–59.
58. Koo EH, Sisodia SS, Archer DR, Martin LJ, Weidemann A, Beyreuther K, Fischer P, Masters CL, Price DL. Precursor of amyloid protein in Alzheimer disease undergoes fast anterograde axonal transport. Proc Natl Acad Sci U S A. 1990;87:1561–5.
59. Lazarov O, Morfini GA, Lee EB, Farah MH, Szodorai A, DeBoer SR, Koliatsos VE, Kins S, Lee VM, Wong PC, et al. Axonal transport, amyloid precursor protein, kinesin-1, and the processing apparatus: revisited. J Neurosci. 2005;25:2386–95.
60. Wang P, Yang G, Mosier DR, Chang P, Zaidi T, Gong YD, Zhao NM, Dominguez B, Lee KF, Gan WB, Zheng H. Defective neuromuscular synapses in mice lacking amyloid precursor protein (APP) and APP-Like protein 2. J Neurosci. 2005;25:1219–25.
61. Klevanski M, Herrmann U, Weyer SW, Fol R, Cartier N, Wolfer DP, Caldwell JH, Korte M, Muller UC. The APP Intracellular Domain Is Required for Normal Synaptic Morphology, Synaptic Plasticity, and Hippocampus-Dependent Behavior. J Neurosci. 2015;35:16018–33.
62. Muller UC, Deller T, Korte M. Not just amyloid: physiological functions of the amyloid precursor protein family. Nat Rev Neurosci. 2017;18:281–98.
63. Wirths O, Weis J, Kayed R, Saido TC, Bayer TA. Age-dependent axonal degeneration in an Alzheimer mouse model. Neurobiol Aging. 2007;28:1689–99.
64. Wirths O, Weis J, Szczygielski J, Multhaup G, Bayer TA. Axonopathy in an APP/PS1 transgenic mouse model of Alzheimer's disease. Acta Neuropathol. 2006;111:312–9.
65. Stone JR, Singleton RH, Povlishock JT. Antibodies to the C-terminus of the beta-amyloid precursor protein (APP): a site specific marker for the detection of traumatic axonal injury. Brain Res. 2000;871:288–302.
66. Hortobagyi T, Wise S, Hunt N, Cary N, Djurovic V, Fegan-Earl A, Shorrock K, Rouse D, Al-Sarraj S. Traumatic axonal damage in the brain can be detected using beta-APP immunohistochemistry within 35 min after head injury to human adults. Neuropathol Appl Neurobiol. 2007;33:226–37.
67. Ruhling S, Kramer F, Schmutz S, Amor S, Jiangshan Z, Schmitz C, Kipp M, Hochstrasser T. Visualization of the Breakdown of the Axonal Transport Machinery: a Comparative Ultrastructural and Immunohistochemical Approach. Mol Neurobiol. 2019;56:3984–98.
68. Ikin AF, Annaert WG, Takei K, De Camilli P, Jahn R, Greengard P, Buxbaum JD. Alzheimer amyloid protein precursor is localized in nerve terminal preparations to Rab5-containing vesicular organelles distinct from those implicated in the synaptic vesicle pathway. J Biol Chem. 1996;271:31783–6.
69. Shapira M, Zhai RG, Dresbach T, Bresler T, Torres VI, Gundelfinger ED, Ziv NE, Garner CC. Unitary assembly of presynaptic active zones from Piccolo-Bassoon transport vesicles. Neuron. 2003;38:237–52.
70. Chiba K, Araseki M, Nozawa K, Furukori K, Araki Y, Matsushima T, Nakaya T, Hata S, Saito Y, Uchida S, et al. Quantitative analysis of APP axonal transport in neurons: role of JIP1 in enhanced APP anterograde transport. Mol Biol Cell. 2014;25:3569–80.

71. Shiff G, Morel N. Rapid anterograde axonal transport of the syntaxin-SNAP 25-VAMP complex. J Neurochem. 1997;68:1663–7.
72. Cai Q, Pan PY, Sheng ZH. Syntabulin-kinesin-1 family member 5B-mediated axonal transport contributes to activity-dependent presynaptic assembly. J Neurosci. 2007;27:7284–96.
73. Forman DS. Axonal transport of mitochondria. Axonal Transp 1987:155–63.
74. Forman DS, Lynch KJ, Smith RS. Organelle dynamics in lobster axons: anterograde, retrograde and stationary mitochondria. Brain Res. 1987;412:96–106.
75. Boldogh IR, Pon LA. Mitochondria on the move. Trends Cell Biol. 2007;17:502–10.
76. Melkov A, Abdu U. Regulation of long-distance transport of mitochondria along microtubules. Cell Mol Life Sci. 2018;75:163–76.
77. Plucinska G, Misgeld T. Imaging of neuronal mitochondria in situ. Curr Opin Neurobiol. 2016;39:152–63.
78. Lautrup S, Sinclair DA, Mattson MP, Fang EF. NAD(+) in Brain Aging and Neurodegenerative Disorders. Cell Metab. 2019;30:630–55.
79. Sasaki Y. Metabolic aspects of neuronal degeneration: From a NAD(+) point of view. Neurosci Res. 2019;139:9–20.
80. Brown EE, Scandura MJ, Pierce EA. Expression of NMNAT1 in the Photoreceptors is Sufficient to Prevent < em > NMNAT1-Associated Disease. *bioRxiv* 2022:2022.2011.2020.517250..
81. Hinckelmann MV, Virlogeux A, Niehage C, Poujol C, Choquet D, Hoflack B, Zala D, Saudou F. Self-propelling vesicles define glycolysis as the minimal energy machinery for neuronal transport. Nat Commun. 2016;7:13233.
82. Cunnane SC, Trushina E, Morland C, Prigione A, Casadesus G, Andrews ZB, Beal MF, Bergersen LH, Brinton RD, de la Monte S, et al. Brain energy rescue: an emerging therapeutic concept for neurodegenerative disorders of ageing. Nat Rev Drug Discov. 2020;19:609–33.
83. Alano CC, Garnier P, Ying W, Higashi Y, Kauppinen TM, Swanson RA. NAD + depletion is necessary and sufficient for poly(ADP-ribose) polymerase-1-mediated neuronal death. J Neurosci. 2010;30:2967–78.
84. Wang S, Xing Z, Vosler PS, Yin H, Li W, Zhang F, Signore AP, Stetler RA, Gao Y, Chen J. Cellular NAD replenishment confers marked neuroprotection against ischemic cell death: role of enhanced DNA repair. Stroke. 2008;39:2587–95.
85. Essuman K, Summers DW, Sasaki Y, Mao X, DiAntonio A, Milbrandt J. The SARM1 Toll/Interleukin-1 Receptor Domain Possesses Intrinsic NAD(+) Cleavage Activity that Promotes Pathological Axonal Degeneration. Neuron. 2017;93:1334–1343e1335.
86. Angeletti C, Amici A, Gilley J, Loreto A, Trapanotto AG, Antoniou C, Merlini E, Coleman MP, Orsomando G. SARM1 is a multi-functional NAD(P)ase with prominent base exchange activity, all regulated by multiple physiologically relevant NAD metabolites. iScience. 2022;25:103812.

87. Figley MD, Gu W, Nanson JD, Shi Y, Sasaki Y, Cunnea K, Malde AK, Jia X, Luo Z, Saikot FK, et al. SARM1 is a metabolic sensor activated by an increased NMN/NAD(+) ratio to trigger axon degeneration. Neuron. 2021;109:1118–1136e1111.
88. Di Stefano M, Nascimento-Ferreira I, Orsomando G, Mori V, Gilley J, Brown R, Janeckova L, Vargas ME, Worrell LA, Loreto A, et al. A rise in NAD precursor nicotinamide mononucleotide (NMN) after injury promotes axon degeneration. Cell Death Differ. 2015;22:731–42.
89. Gilley J, Orsomando G, Nascimento-Ferreira I, Coleman MP. Absence of SARM1 rescues development and survival of NMNAT2-deficient axons. Cell Rep. 2015;10:1974–81.
90. Gilley J, Ribchester RR, Coleman MP. Sarm1 Deletion, but Not Wld^{S}, Confers Lifelong Rescue in a Mouse Model of Severe Axonopathy. Cell Rep. 2017;21:10–6.
91. Mayer PR, Huang N, Dewey CM, Dries DR, Zhang H, Yu G. Expression, localization, and biochemical characterization of nicotinamide mononucleotide adenylyltransferase 2. J Biol Chem. 2010;285:40387–96.
92. Ketschek A, Sainath R, Holland S, Gallo G. The Axonal Glycolytic Pathway Contributes to Sensory Axon Extension and Growth Cone Dynamics. J Neurosci. 2021;41:6637–51.
93. Izadifar A, Courchet J, Virga DM, Verreet T, Hamilton S, Ayaz D, Misbaer A, Vandenbogaerde S, Monteiro L, Petrovic M, et al. Axon morphogenesis and maintenance require an evolutionary conserved safeguard function of Wnk kinases antagonizing Sarm and Axed. Neuron. 2021;109:2864–2883e2868.
94. Turner NL, Macrina T, Bae JA, Yang R, Wilson AM, Schneider-Mizell C, Lee K, Lu R, Wu J, Bodor AL et al. Multiscale and multimodal reconstruction of cortical structure and function. *bioRxiv* 2020:2020.2010.2014.338681..
95. Lewis TL Jr, Turi GF, Kwon SK, Losonczy A, Polleux F. Progressive Decrease of Mitochondrial Motility during Maturation of Cortical Axons In Vitro and In Vivo. Curr Biol. 2016;26:2602–8.
96. Moutaux E, Christaller W, Scaramuzzino C, Genoux A, Charlot B, Cazorla M, Saudou F. Neuronal network maturation differently affects secretory vesicles and mitochondria transport in axons. Sci Rep. 2018;8:13429.
97. Zhou B, Yu P, Lin MY, Sun T, Chen Y, Sheng ZH. Facilitation of axon regeneration by enhancing mitochondrial transport and rescuing energy deficits. J Cell Biol. 2016;214:103–19.
98. Cagin U, Duncan OF, Gatt AP, Dionne MS, Sweeney ST, Bateman JM. Mitochondrial retrograde signaling regulates neuronal function. Proc Natl Acad Sci U S A. 2015;112:E6000–6009.
99. Ibanez CF. Message in a bottle: long-range retrograde signaling in the nervous system. Trends Cell Biol. 2007;17:519–28.
100. Das U, Scott DA, Ganguly A, Koo EH, Tang Y, Roy S. Activity-induced convergence of APP and BACE-1 in acidic microdomains via an endocytosis-dependent pathway. Neuron. 2013;79:447–60.
101. Chidlow G, Ebneter A, Wood JP, Casson RJ. The optic nerve head is the site of axonal transport disruption, axonal cytoskeleton damage and putative axonal regeneration failure in a rat model of

glaucoma. Acta Neuropathol. 2011;121:737–51.

102. Burke S, Trudeau LE. Axonal Domain Structure as a Putative Identifier of Neuron-Specific Vulnerability to Oxidative Stress in Cultured Neurons. *eNeuro* 2022, 9.
103. Giguere N, Delignat-Lavaud B, Herborg F, Voisin A, Li Y, Jacquemet V, Anand-Srivastava M, Gether U, Giros B, Trudeau LE. Increased vulnerability of nigral dopamine neurons after expansion of their axonal arborization size through D2 dopamine receptor conditional knockout. PLoS Genet. 2019;15:e1008352.
104. Guo W, Stoklund Dittlau K, Van Den Bosch L. Axonal transport defects and neurodegeneration: Molecular mechanisms and therapeutic implications. Semin Cell Dev Biol. 2020;99:133–50.
105. Baleriola J, Walker CA, Jean YY, Crary JF, Troy CM, Nagy PL, Hengst U. Axonally synthesized ATF4 transmits a neurodegenerative signal across brain regions. Cell. 2014;158:1159–72.
106. Lamberts JT, Hildebrandt EN, Brundin P. Spreading of alpha-synuclein in the face of axonal transport deficits in Parkinson's disease: a speculative synthesis. Neurobiol Dis. 2015;77:276–83.
107. Wen Y, Parrish JZ, He R, Zhai RG, Kim MD. Nmnat exerts neuroprotective effects in dendrites and axons. Mol Cell Neurosci. 2011;48:1–8.
108. Ji H, Sapar ML, Sarkar A, Wang B, Han C. Phagocytosis and self-destruction break down dendrites of Drosophila sensory neurons at distinct steps of Wallerian degeneration. Proc Natl Acad Sci U S A 2022, 119.
109. Ashrafi G, de Juan-Sanz J, Farrell RJ, Ryan TA. Molecular Tuning of the Axonal Mitochondrial Ca(2+) Uniporter Ensures Metabolic Flexibility of Neurotransmission. Neuron. 2020;105:678–687e675.
110. Zampese E, Wokosin DL, Gonzalez-Rodriguez P, Guzman JN, Tkatch T, Kondapalli J, Surmeier WC, D'Alessandro KB, De Stefani D, Rizzuto R, et al. Ca(2+) channels couple spiking to mitochondrial metabolism in substantia nigra dopaminergic neurons. Sci Adv. 2022;8:eabp8701.
111. Perez-Liebana I, Juaristi I, Gonzalez-Sanchez P, Gonzalez-Moreno L, Rial E, Podunavac M, Zakarian A, Molgo J, Vallejo-Illarramendi A, Mosqueira-Martin L, et al. A Ca(2+)-Dependent Mechanism Boosting Glycolysis and OXPHOS by Activating Aralar-Malate-Aspartate Shuttle, upon Neuronal Stimulation. J Neurosci. 2022;42:3879–95.
112. Yu SB, Sanchez RG, Papich ZD, Whisenant TC, Ghassemian M, Koberstein JN, Stewart ML, Pekkurnaz G. Neuronal activity-driven O-GlcNAcylation promotes mitochondrial plasticity. *bioRxiv* 2023:2023.2001.2011.523512..
113. Pekkurnaz G, Trinidad JC, Wang X, Kong D, Schwarz TL. Glucose regulates mitochondrial motility via Milton modification by O-GlcNAc transferase. Cell. 2014;158:54–68.
114. Mor DE, Sohrabi S, Kaletsky R, Keyes W, Tartici A, Kalia V, Miller GW, Murphy CT. Metformin rescues Parkinson's disease phenotypes caused by hyperactive mitochondria. Proc Natl Acad Sci U S A. 2020;117:26438–47.
115. Soman SK, Bazala M, Keatinge M, Bandmann O, Kuznicki J. Restriction of mitochondrial calcium overload by mcu inactivation renders a neuroprotective effect in zebrafish models of Parkinson's disease. Biol Open 2019, 8.

116. Calvo-Rodriguez M, Hou SS, Snyder AC, Kharitonova EK, Russ AN, Das S, Fan Z, Muzikansky A, Garcia-Alloza M, Serrano-Pozo A, et al. Increased mitochondrial calcium levels associated with neuronal death in a mouse model of Alzheimer's disease. Nat Commun. 2020;11:2146.
117. Osterloh JM, Yang J, Rooney TM, Fox AN, Adalbert R, Powell EH, Sheehan AE, Avery MA, Hackett R, Logan MA, et al. dSarm/Sarm1 is required for activation of an injury-induced axon death pathway. Science. 2012;337:481–4.
118. Murata H, Sakaguchi M, Kataoka K, Huh NH. SARM1 and TRAF6 bind to and stabilize PINK1 on depolarized mitochondria. Mol Biol Cell. 2013;24:2772–84.
119. Gerdts J, Summers DW, Sasaki Y, DiAntonio A, Milbrandt J. Sarm1-mediated axon degeneration requires both SAM and TIR interactions. J Neurosci. 2013;33:13569–80.
120. Murata H, Khine CC, Nishikawa A, Yamamoto KI, Kinoshita R, Sakaguchi M. c-Jun N-terminal kinase (JNK)-mediated phosphorylation of SARM1 regulates NAD(+) cleavage activity to inhibit mitochondrial respiration. J Biol Chem. 2018;293:18933–43.
121. Ko KW, Devault L, Sasaki Y, Milbrandt J, DiAntonio A. Live imaging reveals the cellular events downstream of SARM1 activation. Elife 2021, 10.
122. Sato-Yamada Y, Strickland A, Sasaki Y, Bloom J, DiAntonio A, Milbrandt J. A SARM1-mitochondrial feedback loop drives neuropathogenesis in a Charcot-Marie-Tooth disease type 2A rat model. J Clin Invest 2022, 132.
123. Reiman EM, Caselli RJ, Yun LS, Chen K, Bandy D, Minoshima S, Thibodeau SN, Osborne D. Preclinical evidence of Alzheimer's disease in persons homozygous for the ε4 allele for apolipoprotein E. J New England Journal of Medicine. 1996;334:752–8.
124. Ye F, Funk Q, Rockers E, Shulman JM, Masdeu JC, Pascual B. Alzheimer's Disease Neuroimaging I: In Alzheimer-prone brain regions, metabolism and risk-gene expression are strongly correlated. Brain Commun. 2022;4:fcac216.
125. Ciarmiello A, Cannella M, Lastoria S, Simonelli M, Frati L, Rubinsztein DC, Squitieri F. Brain white-matter volume loss and glucose hypometabolism precede the clinical symptoms of Huntington's disease. J Nucl Med. 2006;47:215–22.
126. Diehl-Schmid J, Licata A, Goldhardt O, Forstl H, Yakushew I, Otto M, Anderl-Straub S, Beer A, Ludolph AC, Landwehrmeyer GB, et al. FDG-PET underscores the key role of the thalamus in frontotemporal lobar degeneration caused by C9ORF72 mutations. Transl Psychiatry. 2019;9:54.
127. Cistaro A, Valentini MC, Chio A, Nobili F, Calvo A, Moglia C, Montuschi A, Morbelli S, Salmaso D, Fania P, et al. Brain hypermetabolism in amyotrophic lateral sclerosis: a FDG PET study in ALS of spinal and bulbar onset. Eur J Nucl Med Mol Imaging. 2012;39:251–9.
128. Matthews DC, Lerman H, Lukic A, Andrews RD, Mirelman A, Wernick MN, Giladi N, Strother SC, Evans KC, Cedarbaum JM, Even-Sapir E. FDG PET Parkinson's disease-related pattern as a biomarker for clinical trials in early stage disease. Neuroimage Clin. 2018;20:572–9.
129. Kalpouzos G, Chetelat G, Baron JC, Landeau B, Mevel K, Godeau C, Barre L, Constans JM, Viader F, Eustache F, Desgranges B. Voxel-based mapping of brain gray matter volume and glucose

metabolism profiles in normal aging. Neurobiol Aging. 2009;30:112–24.

130. Oh H, Madison C, Baker S, Rabinovici G, Jagust W. Dynamic relationships between age, amyloid-beta deposition, and glucose metabolism link to the regional vulnerability to Alzheimer's disease. Brain. 2016;139:2275–89.
131. Krell-Roesch J, Syrjanen JA, Vassilaki M, Lowe VJ, Vemuri P, Mielke MM, Machulda MM, Stokin GB, Christianson TJ, Kremers WK, et al. Brain Regional Glucose Metabolism, Neuropsychiatric Symptoms, and the Risk of Incident Mild Cognitive Impairment: The Mayo Clinic Study of Aging. Am J Geriatr Psychiatry. 2021;29:179–91.
132. Baran TM, Lin FV, Alzheimer's Disease Neuroimaging I. Amyloid and FDG PET of Successful Cognitive Aging: Global and Cingulate-Specific Differences. J Alzheimers Dis. 2018;66:307–18.
133. Kelley CM, Ginsberg SD, Liang WS, Counts SE, Mufson EJ. Posterior cingulate cortex reveals an expression profile of resilience in cognitively intact elders. Brain Commun. 2022;4:fcac162.
134. Leech R, Sharp DJ. The role of the posterior cingulate cortex in cognition and disease. Brain. 2014;137:12–32.
135. Crossley NA, Mechelli A, Scott J, Carletti F, Fox PT, McGuire P, Bullmore ET. The hubs of the human connectome are generally implicated in the anatomy of brain disorders. Brain. 2014;137:2382–95.
136. Yu M, Sporns O, Saykin AJ. The human connectome in Alzheimer disease - relationship to biomarkers and genetics. Nat Rev Neurol. 2021;17:545–63.
137. Hagmann P, Cammoun L, Gigandet X, Meuli R, Honey CJ, Wedeen VJ, Sporns O. Mapping the structural core of human cerebral cortex. PLoS Biol. 2008;6:e159.
138. Mito R, Raffelt D, Dhollander T, Vaughan DN, Tournier JD, Salvado O, Brodtmann A, Rowe CC, Villemagne VL, Connelly A. Fibre-specific white matter reductions in Alzheimer's disease and mild cognitive impairment. Brain. 2018;141:888–902.
139. Xu Z, Xia M, Wang X, Liao X, Zhao T, He Y. Meta-connectomic analysis maps consistent, reproducible, and transcriptionally relevant functional connectome hubs in the human brain. Commun Biol. 2022;5:1056.
140. Goyal MS, Vlassenko AG, Blazey TM, Su Y, Couture LE, Durbin TJ, Bateman RJ, Benzinger TL, Morris JC, Raichle ME. Loss of Brain Aerobic Glycolysis in Normal Human Aging. Cell Metab. 2017;26:353–360e353.
141. Vlassenko AG, Gordon BA, Goyal MS, Su Y, Blazey TM, Durbin TJ, Couture LE, Christensen JJ, Jafri H, Morris JC, et al. Aerobic glycolysis and tau deposition in preclinical Alzheimer's disease. Neurobiol Aging. 2018;67:95–8.
142. Goyal MS, Blazey T, Metcalf NV, McAvoy MP, Strain J, Rahmani M, Durbin TJ, Xiong C, Benzinger TL-S, Morris JC et al. Brain aerobic glycolysis and resilience in Alzheimer disease. *bioRxiv* 2022:2022.2006.2021.497006..
143. Hou Y, Wei Y, Lautrup S, Yang B, Wang Y, Cordonnier S, Mattson MP, Croteau DL, Bohr VA. NAD(+) supplementation reduces neuroinflammation and cell senescence in a transgenic mouse model of Alzheimer's disease via cGAS-STING. Proc Natl Acad Sci U S A 2021, 118.

144. Harlan BA, Killoy KM, Pehar M, Liu L, Auwerx J, Vargas MR. Evaluation of the NAD(+) biosynthetic pathway in ALS patients and effect of modulating NAD(+) levels in hSOD1-linked ALS mouse models. Exp Neurol. 2020;327:113219.
145. Gautam M, Gunay A, Chandel NS, Ozdinler PH. Mitochondrial dysregulation occurs early in ALS motor cortex with TDP-43 pathology and suggests maintaining NAD(+) balance as a therapeutic strategy. Sci Rep. 2022;12:4287.
146. Ljungberg MC, Ali YO, Zhu J, Wu CS, Oka K, Zhai RG, Lu HC. CREB-activity and nmnat2 transcription are down-regulated prior to neurodegeneration, while NMNAT2 over-expression is neuroprotective, in a mouse model of human tauopathy. Hum Mol Genet. 2012;21:251–67.
147. Cheng XS, Shi FX, Zhao KP, Lin W, Li XY, Zhang J, Bu YY, Zhu R, Li XH, Duan DX, et al. Nmnat2 attenuates amyloidogenesis and up-regulates ADAM10 in AMPK activity-dependent manner. Aging. 2021;13:23620–36.
148. Fang F, Zhuang P, Feng X, Liu P, Liu D, Huang H, Li L, Chen W, Liu L, Sun Y, et al. NMNAT2 is downregulated in glaucomatous RGCs, and RGC-specific gene therapy rescues neurodegeneration and visual function. Mol Ther. 2022;30:1421–31.
149. Ren MYY, Heng KHY, Ng LY, Chong CY, Ng YT, Gorur-Shandilya S, Lee RMQ, Lim KL, Zhang J, Koh TW. MED13 and glycolysis are conserved modifiers of α-synuclein-associated neurodegeneration. Cell Rep. 2022;41(12):111852.
150. Manzo E, Lorenzini I, Barrameda D, O'Conner AG, Barrows JM, Starr A, Kovalik T, Rabichow BE, Lehmkuhl EM, Shreiner DD et al. Glycolysis upregulation is neuroprotective as a compensatory mechanism in ALS. Elife 2019, 8.

Figures

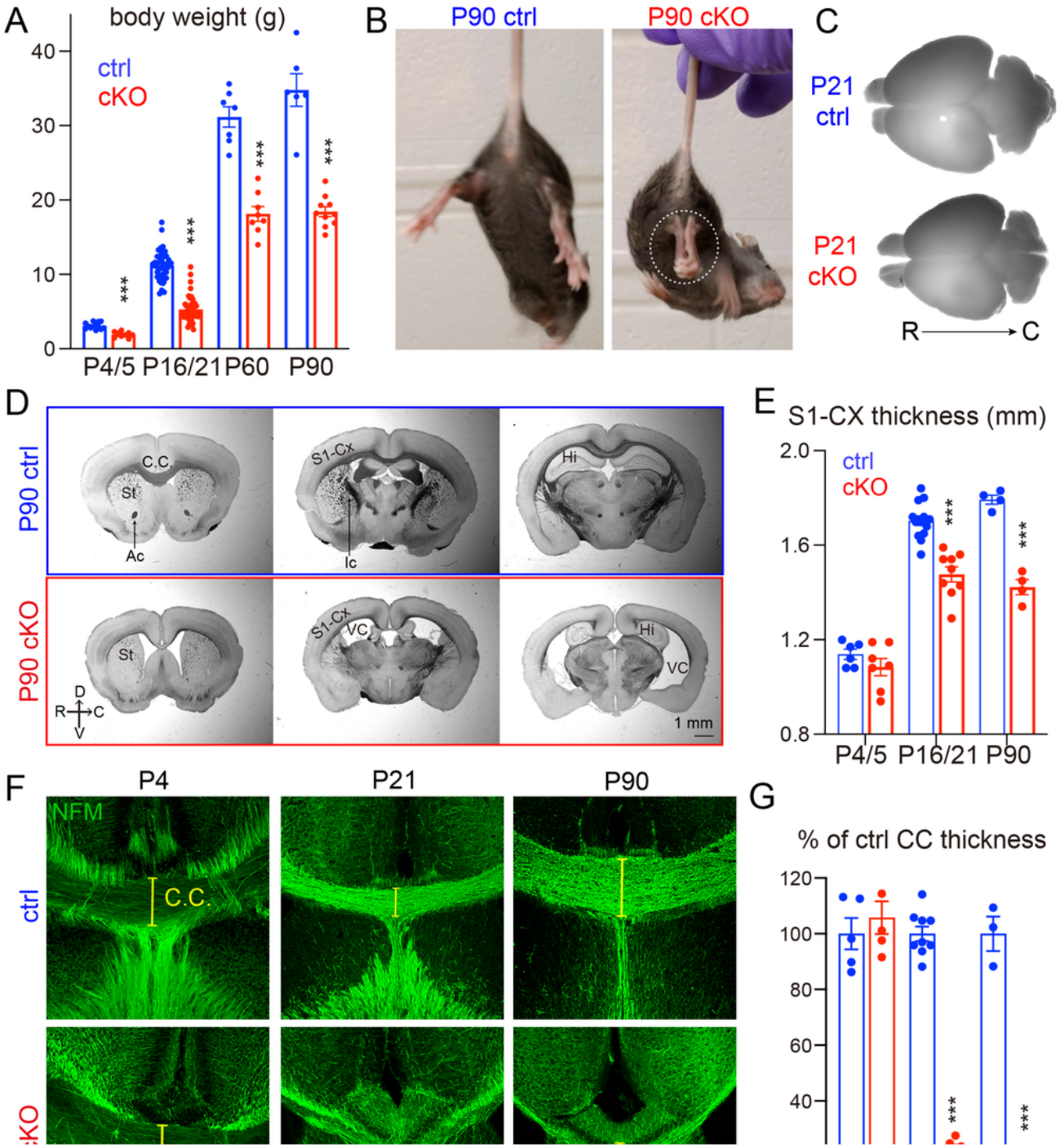

Figure 1

Deleting NMNAT2 in cortical glutamatergic neurons results in age-dependent axonal degeneration

(**A**) Body weight of cKO and their littermate control (ctrl) mice at P4, P16/21, P60, and P90. Mice numbers: P4/5, 13 ctrl and 9 cKO; P16/P21 43 ctrl and 46 cKO; P60, 7 ctrl and 8 cKO; P90, 6 ctrl and 10 cKO. (**B**) Movie screenshots showing that a P90 cKO mouse exhibits hindlimb clasping behaviors (dashed

white oval), a classic motor deficit observed in many neurodegenerative models (see Sup. Movies), but not in a ctrl mouse. (**C, D**) Bright field images showing whole brains and coronal plane brain sections (rostral to caudal from left to right) from ctrl and cKO mice. In addition to the smaller brain sizes, cKO brains have enlarged ventricles and reduced cortical regions and hippocampal areas. (**E**) Quantification of the primary somatosensory (S1) cortex thickness in ctrl and cKO mice at different ages. Mice numbers: P4/5, 6 ctrl and 7 cKO; P16/P21, 14 ctrl and 9 cKO; P90, 4 ctrl and 4 cKO. (**F**) Confocal images of immunohistochemical staining of NFM (medium-size neurofilament) showing axonal tracts through the corpus callosum (CC) in ctrl and cKO brains at P4, P21, and P90. Yellow brackets mark the thickness of the CC. (**G**) Quantification of the CC thickness, normalized to its value in ctrl mice. Mice numbers: P4/5, 5 ctrl and 5 cKO; P16/P21, 9 ctrl and 7 cKO; P90, 3 ctrl and 3 cKO. Abbreviations: Ac, anterior commissure; Ic, internal capsule; CC, corpus callosum; Cx, cortex; Hi, hippocampus; St, striatum; VC, ventricle. Unpaired t-test and Mann-Whitney test were applied for the statistic result, ***p<0.001, ****p<0.0001.

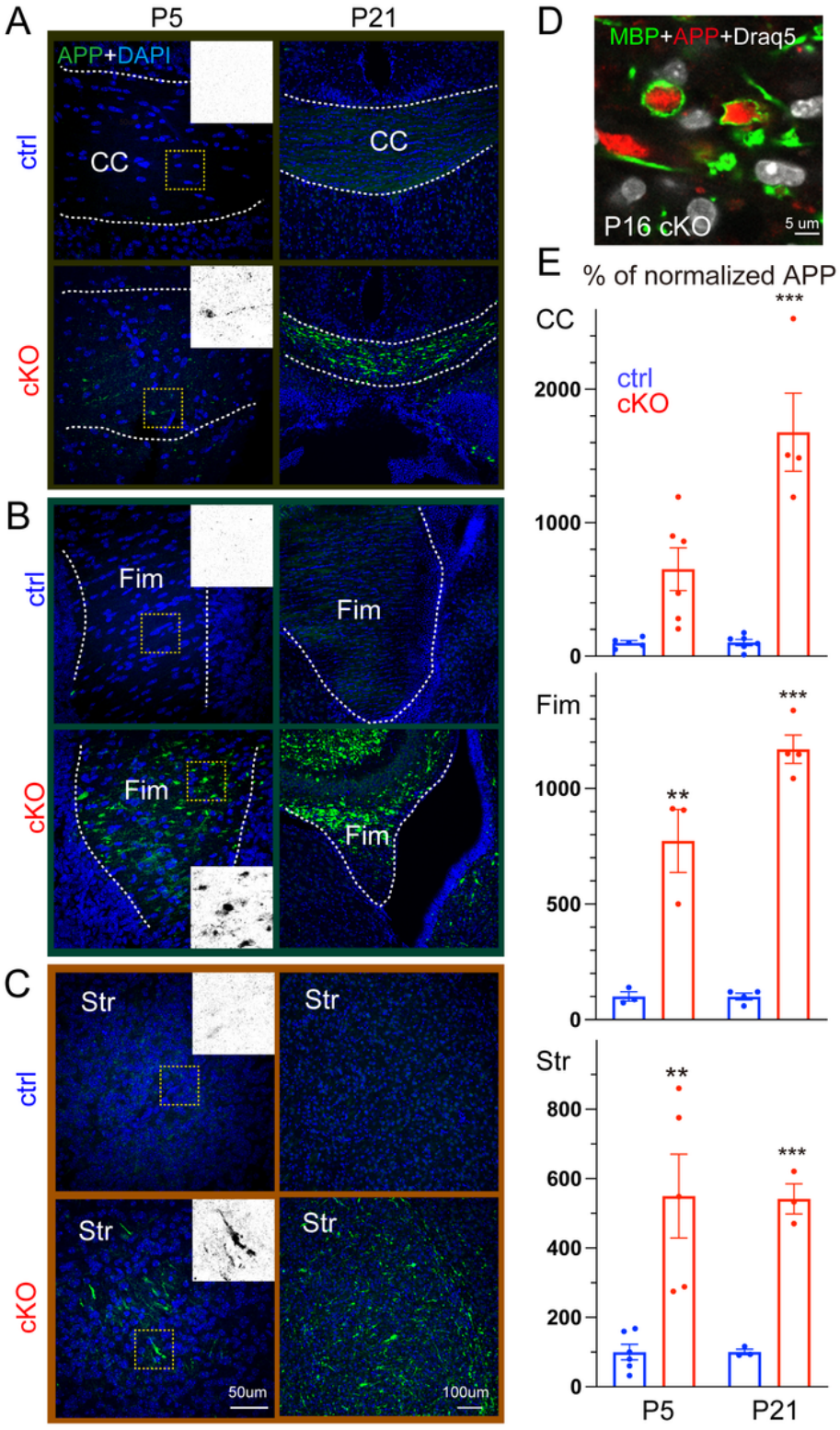

Figure 2

Deleting NMNAT2 in cortical glutamatergic neurons results in Amyloid Precursor Protein (APP) accumulation

(**A, B, C**) Representative confocal microscopy images showing APP accumulation in multiple brain regions of ctrl and cKO mice at P5 and P21. Scale bars, 50 um for all left panels, 100 um for all right

panels. Dashed white lines mark the margins of corpus callosum (A) and fimbria (B). (**D**) High magnification image showing that the accumulated APP is encircled by myelin sheath labeled by myelin basic protein (MBP) staining in P16 cKO corpus callosum (observed in 3 out of 3 cKO brains). (**E**) Quantification of the APP signal in the corpus callosum, hippocampal fimbria, and striatum area of cKO mice normalized to the average signal in ctrl mice at P5 and P21. Number of mice: P5, 3-6 ctrl, and 3-6 cKO; P16/P21 3-6 ctrl and 3-4 cKO. Unpaired t-test and Mann-Whitney test were applied for the statistic result, *p<0.05, **p<0.01, ***p<0.001.

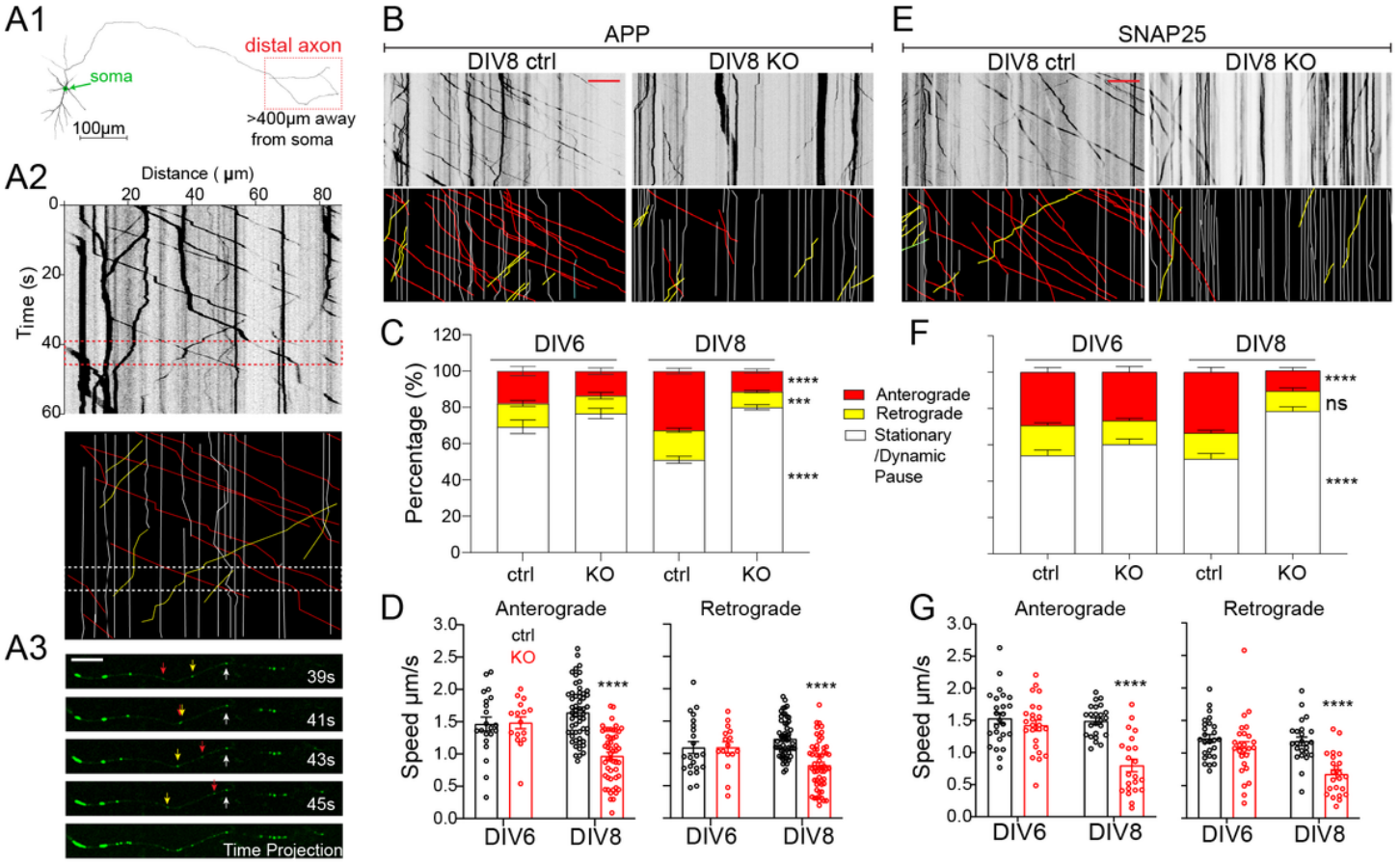

Figure 3

Nmnat2 is required for transporting vesicular cargos in the distal axon

(A1) Diagram indicating the distal axon region (> 400 μm from the soma) where axonal transport was examined with time-lapse imaging. **(A2)** Example kymograph (upper) and annotations (lower) with anterograde (red lines), retrograde (yellow lines), and stationary/dynamic pause (white lines) movements indicated. **(A3)** Four image examples showing APP-EGFP movement along an axon segment during the times indicated in the dashed box in **A2**. Scale bar, 10 μm. **(B, E)**Representative kymographs for APP-EGFP and SNAP25-EGFP from DIV8 ctrl and KO distal axons. Scale bar, 20 μm. **(C, F)** Percentages of APP- or SNAP25-EGFP vesicles moving antero/retrogradely or staying stationary/dynamic pause in ctrl and KO neurons. Numbers (neurons imaged) and statistics: **(C)**DIV6, 22 ctrl, and 19 KO; DIV8, 56 ctrl, and 62 KO; compared with two-way ANOVA and Šídák's multiple comparisons for anterograde and

stationary/dynamic pause categories, compared with multiple Mann-Whitney test and Holm-Šídák multiple comparisons for the retrograde category. **(F)**DIV6, 27 ctrl, 26 KO; DIV8, 24 ctrl, 27 KO; two-way ANOVA with Tukey's multiple comparisons. **(D, G)** Velocity of antero- and retrograde transport in ctrl and KO neurons from 2-3 independent experiments. Numbers (neurons imaged) and statistics: **(D)** Anterograde velocity analysis: DIV6, 21 ctrl and 16 KO; DIV8, 56 ctrl and 51 KO. Retrograde velocity analysis: DIV6: 22 ctrl, 16 KO; DIV8, 56 ctrl, 58 KO. Two-way ANOVA with Šídák's multiple comparisons. **(G)** Anterograde velocity analysis: DIV6, 25 ctrl, 24 KO; DIV8, 24 ctrl, 22 KO; two-way ANOVA with Tukey's multiple comparisons. Retrograde velocity analysis: DIV6, 25 ctrl, 26 KO; DIV8, 24 ctrl, 23 KO; multiple Mann-Whitney test with Holm-Šídák multiple comparisons. KO was compared to ctrl of the same DIV in all data sets. Data represent mean ± SEM, ****p<0.0001. APP and SNAP25 data were collected from 3 and 2 independent experiments, respectively.

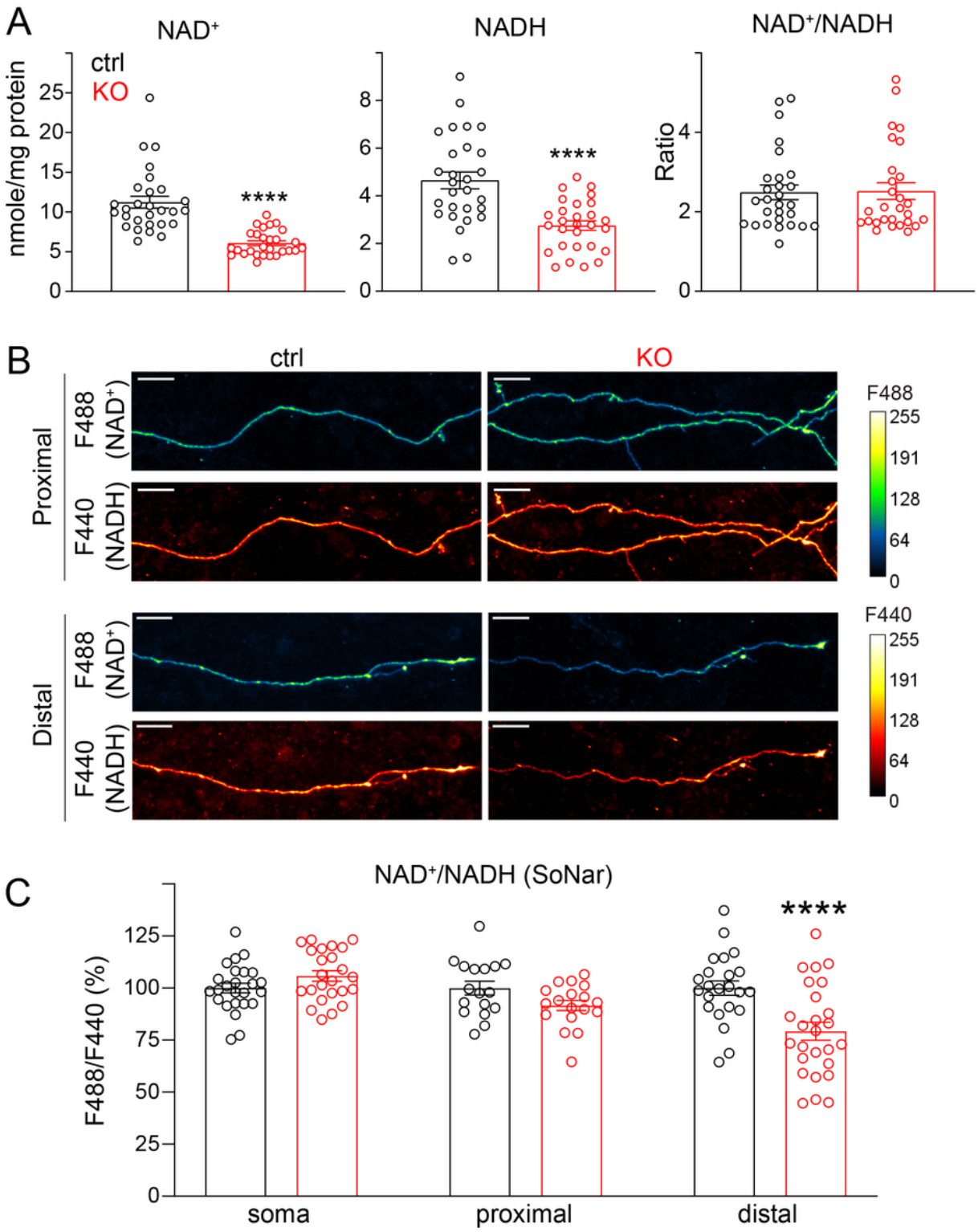

Figure 4

Loss of NMNAT2 reduces NAD$^+$ levels and impairs the NAD redox potential in distal axons

(A) Levels of NAD$^+$ and NADH and calculated NAD$^+$/NADH ratios in DIV8 ctrl and KO cortical neurons as measured by the NAD$^+$/NADH-Glo assay and normalized to protein amounts. Readings from 28 ctrl and 28 KO culture wells from 4 independent culture experiments; unpaired t-test was used for NADH while

Mann-Whitney test was used for both NAD^+ and NAD^+/NADH ratios due to their distributions. **(B)** Representative images showing signals emitted from the SoNar (NAD^+/NADH) ratiometric sensor for NAD^+ and NADH in the proximal and distal axons of DIV 8 ctrl or KO cortical neurons. Scale bar, 20 um. **(C)** NAD+/NADH ratios in soma, proximal and distal axons of DIV7 and 8 ctrl and KO cortical neurons revealed by F488/F440 ratiometric measurements of the SoNar sensor (Soma: 25 ctrl and 24 KO from 2 independent experiments; proximal axon segments: 19 ctrl and 20 KO from 3 independent experiments; distal axon segments: 26 ctrl and 30 KO from 3 independent experiments; two-way ANOVA with Tukey's multiple comparisons test). All above data represents mean ± SEM, ****p<0.0001.

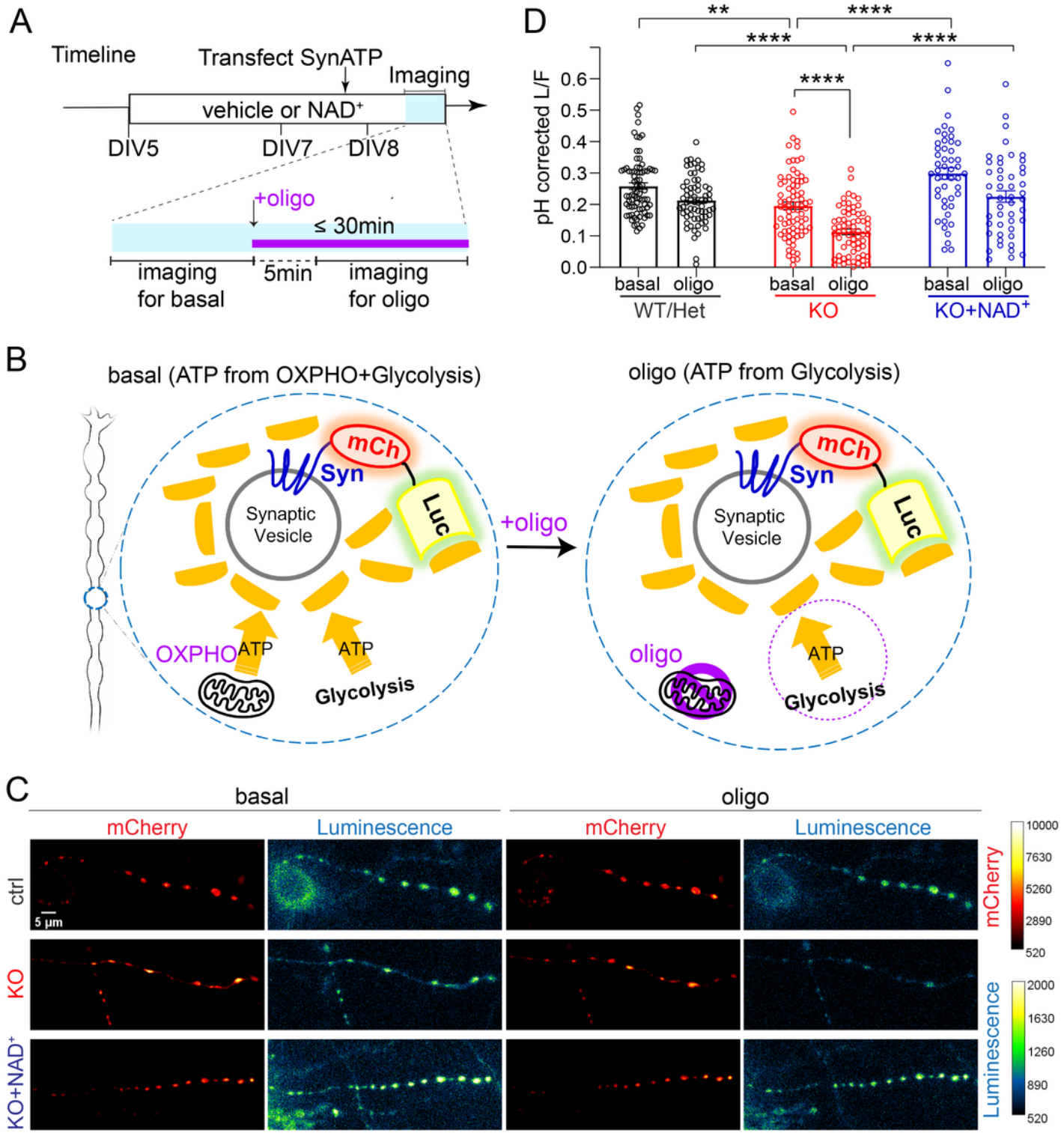

Figure 5

NMNAT2 loss impairs glycolysis in distal axon presynaptic varicosities

(A) Schematic diagram of the Syn-ATP sensor configuration and the treatment and imaging timeline. Syn: synaptophysin, mCh: mCherry, Luc: luciferase. **(B)** Representative Syn-ATP luminescence and fluorescence images of distal axon varicosities under basal and oligomycin-treatment conditions from

DIV8 ctrl, KO, and KO neurons supplemented with NAD^+ (KO+NAD^+). Scale bar, 5 µm. **(C)** pH-corrected L/F (Luminescence/Fluorescence) ratio representing relative presynaptic ATP levels measured by the Syn-ATP sensor in mCherry positive varicosities of distal axons of DIV8 ctrl, KO, and KO+NAD^+ neurons. Numbers (neurons imaged) and statistics: 78 ctrl, 77 KO, and 48 KO+NAD^+ under basal conditions; 67 ctrl, 68 KO, and 48 KO+NAD^+ under oligomycin-treated conditions. Ctrl and KO were from 5 independent experiments, and KO+NAD^+ was from 2 independent experiments. Kruskal-Wallis test with Dunn's multiple comparisons test was used. All above data represents mean ± SEM, ** p=0.004, ****p<0.0001. In the NAD^+ treated KO group, the difference between basal and oligomycin treatment conditions is marginal to significance, p= 0.0537.

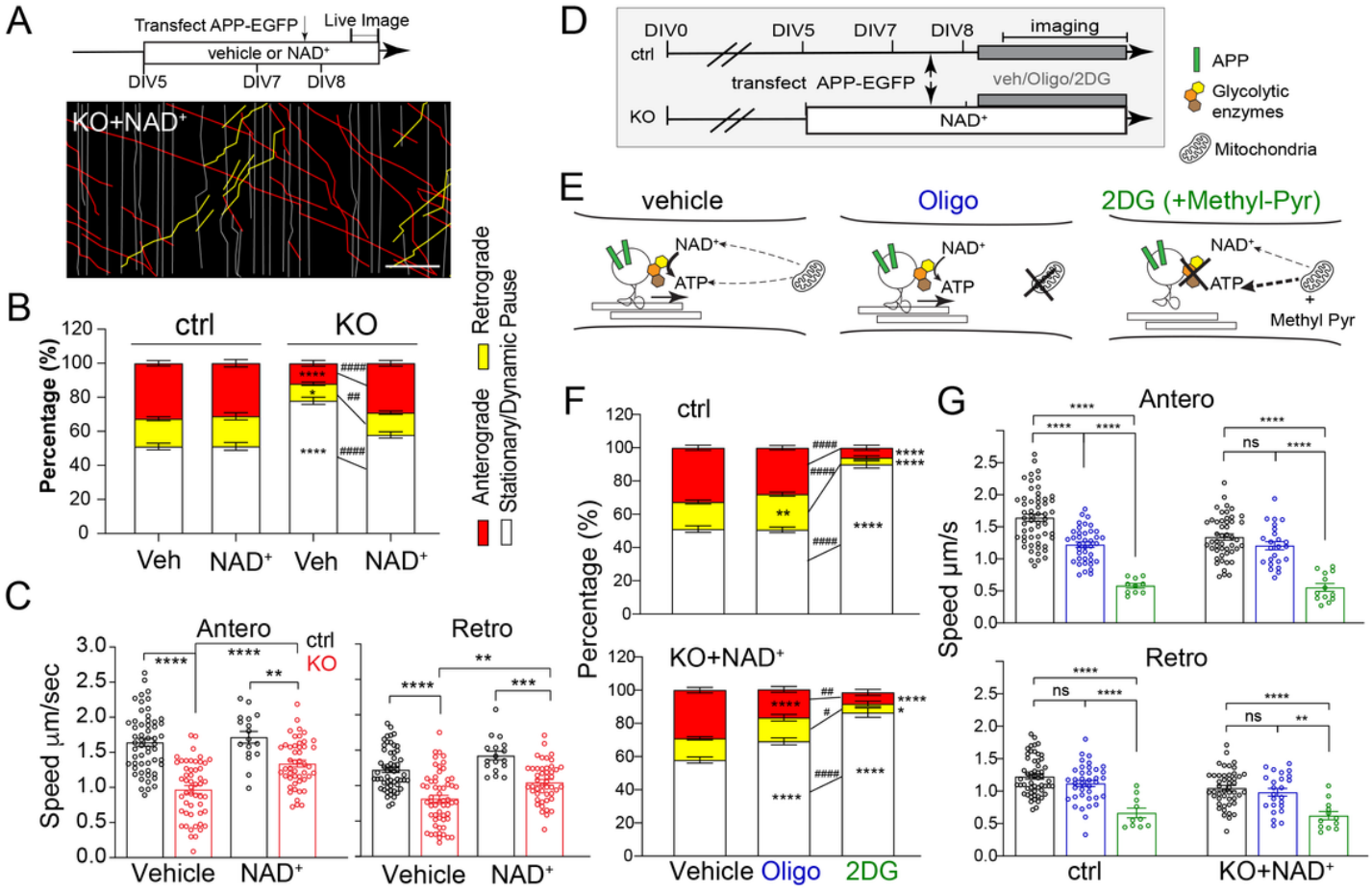

Figure 6

NAD^+ supplementation depends on glycolysis to rescue APP transport in NMNAT2 KO neurons

(A) Representative kymographs from DIV8 ctrl or KO neurons supplemented with Veh (vehicle) or 1 mM NAD^+ since DIV5. Scale bar, 20 µm. **(B)** Percentages of APP-EGFP vesicles moving anterogradely, retrogradely, or pausing in distal axons of DIV8 ctrl and KO neurons supplemented with Veh or NAD^+. Numbers (neurons imaged) and statistics: 56 ctrl+Veh, 62 KO+Veh, 17 ctrl+NAD^+,and 49 KO+NAD^+, *p= 0.0232, $^{\#\#}$p= 0.0018. Significant comparison to ctrl+Veh and KO+Veh groups was labeled with* and $^{\#}$,

respectively. **(C)** Velocity of antero- and retrograde transport of APP-EGFP in distal axons of DIV8 ctrl and KO neurons supplemented with Veh or NAD^+. Numbers (neurons imaged) and statistics: 56 ctrl+Veh, 51-58 KO+Veh, 17 ctrl+NAD^+, and 47-48 KO+NAD^+ for anterograde velocity, (anterograde) **p= 0.0041, (retrograde) **p= 0.0013, ***p= 0.0002. **(E)** Schematic representation of how glycolysis and mitochondrial respiration are affected by Oligo or 2DG(+Methyl-Pyr) treatment. **(F)** Percentages of APP-EGFP vesicles moving anterogradely, retrogradely, or pausing in distal axons of DIV8 ctrl and KO+NAD^+ neurons in the presence of vehicle, Oligo, or 2DG. Numbers (neurons imaged) and statistics: 56 ctrl+Veh, 39 ctrl+oligo, and 20 ctrl+2DG, **p=0.0059; 49 KO+NAD^++Veh, 22-25 KO+NAD^++Oligo,and 15-18 KO+NAD^++2DG, *p= 0.0291, $^{\#}$p= 0.0252. Significant comparisons to Veh-treated and Oligo-treated groups were labeled with * and $^{\#,}$ respectively. **(G)** Velocity of antero- and retrograde transport of APP-EGFP in distal axons of DIV8 ctrl and KO+NAD^+ neurons in the presence of vehicle, Oligo, or 2DG. Numbers (neurons imaged) and statistics: 56 ctrl+Veh, 38-39 ctrl+oligo, 10 ctrl+2DG, 47-48 KO+NAD^+, 24 KO+NAD^++Oligo, and 12-13 KO+NAD^++2DG, **p=0.0011. All above data represent mean ± SEM, two-way ANOVA with Tukey's multiple comparisons test or Kruskal-Wallis test with Dunn's multiple comparisons test were used, see details in supplemented excel, ****p<0.0001, $^{\#\#\#\#}$p<0.0001.

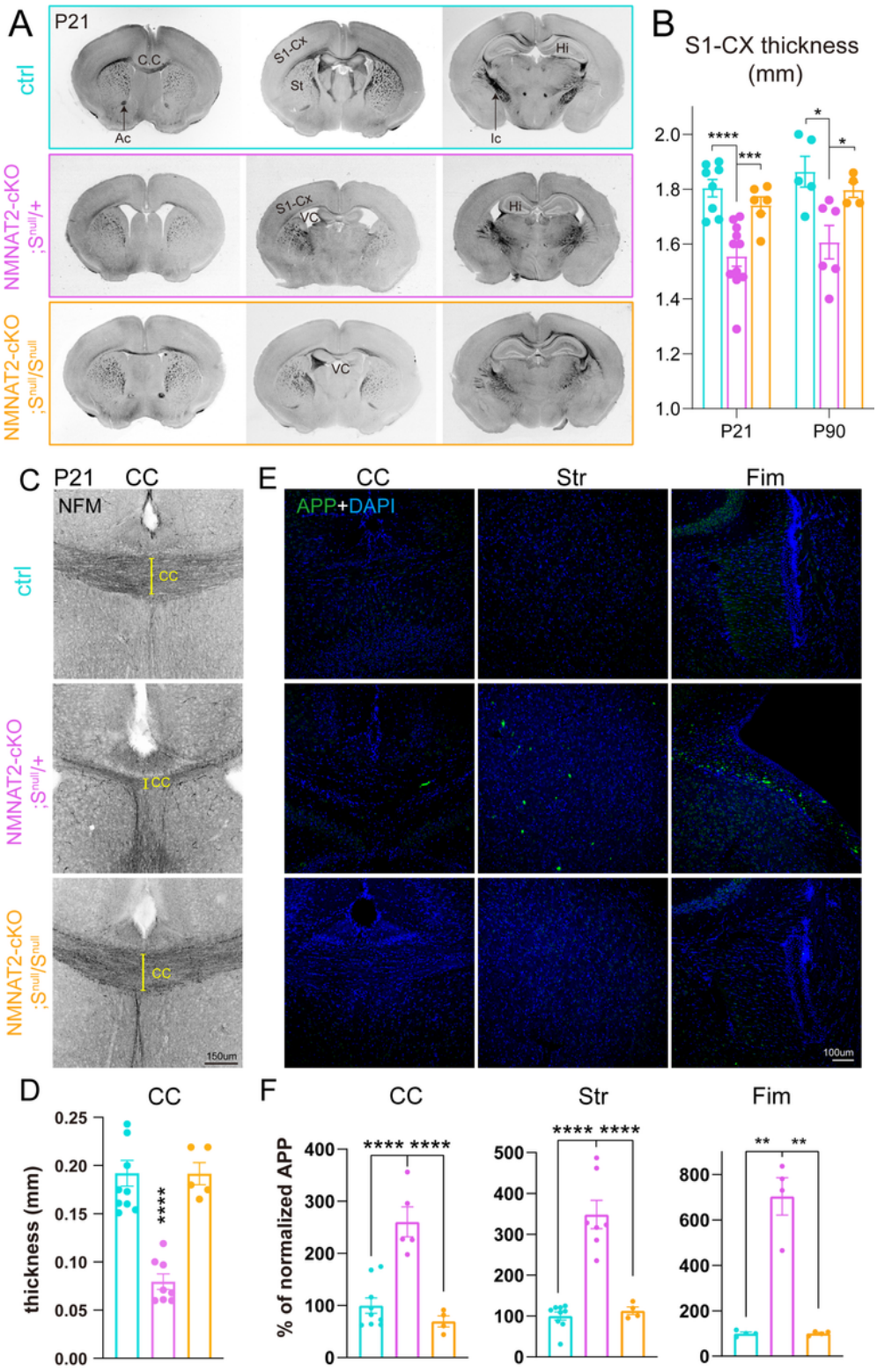

Figure 7

Deleting SARM1 prevents neurodegenerative phenotypes in NMNAT2 cKO brains.

(**A**) Bright field images of coronal brain sections (rostral to caudal from left to right) from ctrl, NMNAT2 cKO; S^{null}/+, and NMNAT2 cKO; S^{null}/S^{null} mice. Enlarged ventricle, greatly reduced corpus callosum, and internal capsule were evident in NMNAT2 cKO; S^{null}/+ but not in NMNAT2 cKO; S^{null}/S^{null} brains. (**B**)

Thickness of the primary somatosensory cortex in P16/21 and P90 mice. Number of mice: P16/21, 8 ctrl, 11 NMNAT2 cKO; S^{null}/+, 6 NMNAT2 cKO; S^{null}/S^{null}; P90, 5 ctrl, 6 NMNAT2 cKO; S^{null}/+, 4 NMNAT2 cKO; S^{null}/S^{null}. ***, p=0.0018, q=0.0009. (Ctrl vs. NMNAT2 cKO; S^{null}/+) *, p= 0.0049, q= 0.0103. (NMNAT2 cKO; S^{null}/+ vs. NMNAT2 cKO; S^{null}/S^{null}) *, p= 0.0341, q= 0.0358. (**C**) Representative NF-M (black) immunostaining images showing corpus callosum around the midline area in ctrl, NMNAT2 cKO; S^{null}/+, and NMNAT2 cKO; S^{null}/S^{null} rostral brain section at P21. (**D**) CC thickness quantification. Number of mice: P21, 10 ctrl, 8 NMNAT2 cKO; S^{null}/+, 5 NMNAT2 cKO; S^{null}/S^{null}. (**E**) Immunohistology images showing APP accumulation in the corpus callosum, fimbria, and striatum of P21 NMNAT2 cKO; S^{null}/+, but not in ctrl and NMNAT2 cKO; S^{null}/S^{null} brains. (**F**) Quantification of the APP signal in the brain regions shown in (E) normalized to the value in ctrl mice. Number of mice: 7-9 ctrl, 4-5 NMNAT2 cKO; S^{null}/+, 4 NMNAT2 cKO; S^{null}/S^{null}. CC, corpus callosum; Str, striatum; Fim, Fimbria. (Fim Ctrl vs. NMNAT2 cKO; S^{null}/+) **, p=0.0186, q= 0.0098. (NMNAT2 cKO; S^{null}/+ vs. NMNAT2 cKO; S^{null}/S^{null}) **, p=0.0186, q=0.0098. All above data represent mean ± SEM. One-way ANOVA with a two-stage linear step-up procedure of Benjamini, Krieger, and Yekutieli was used, ****p<0.0001.

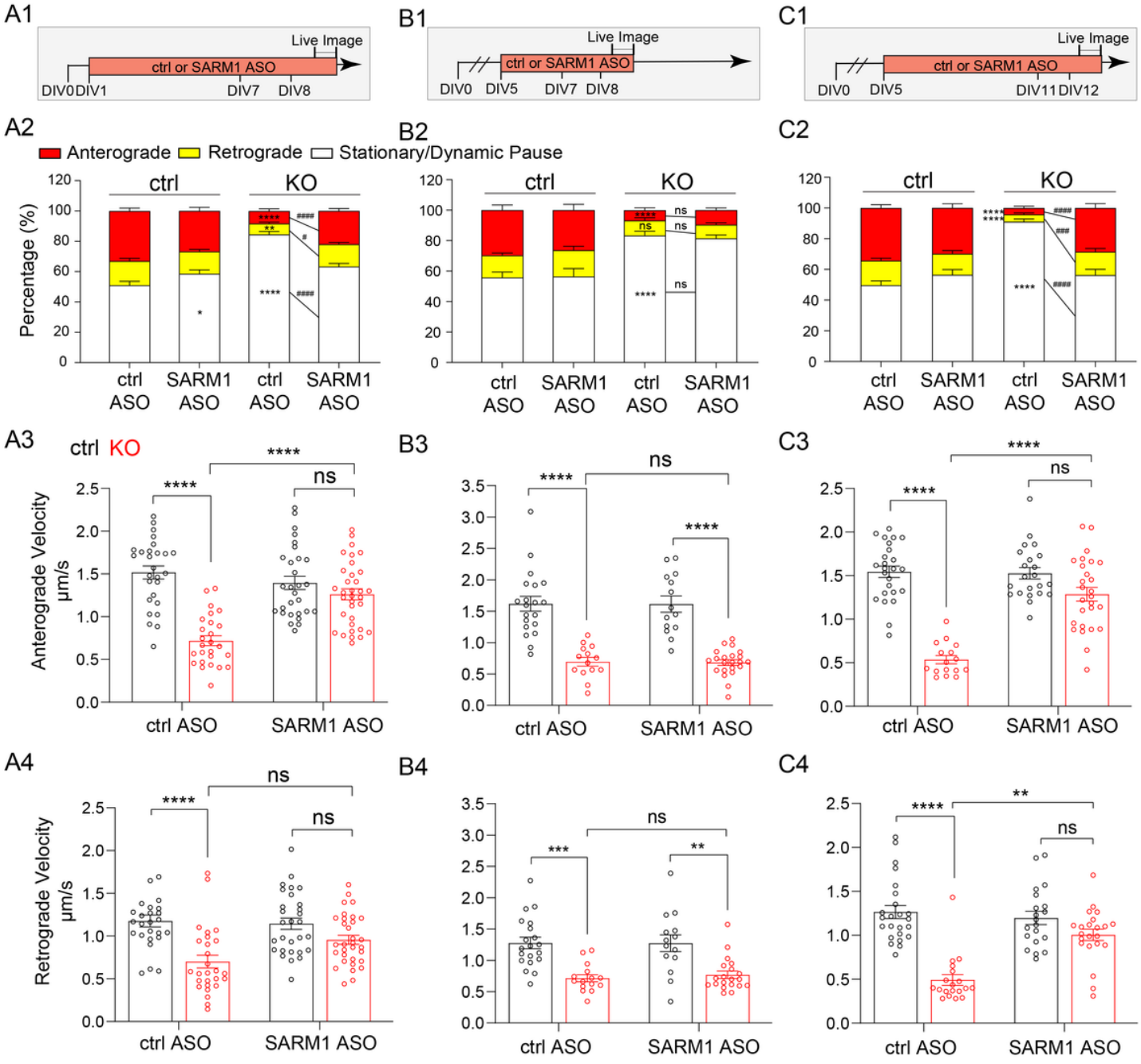

Figure 8

SARM1 knockdown restores APP axonal transport in NMNAT2 KO neurons

(A1, B1, C1) Experimental timeline. **(A2, B2, C2)** Percentages of APP vesicles moving anterogradely, retrogradely, or staying stationary in distal axons of ctrl and KO neurons following the treatments indicated in **A1, B1, and C1,** respectively. Numbers of neurons imaged and statistics: (**A2**) 27 ctrl+ctrl ASO, 31 KO+ctrl ASO, 29 ctrl+SARM1 ASO, and 33 KO+SARM1 ASO, *p= 0.0286, $^{\#}$p= 0.018, **p= 0.0069. (**B2**) 20 ctrl+ctrl ASO, 22 KO+ctrl ASO, 14 ctrl+SARM1 ASO, and 26 KO+SARM1 ASO. (**C2**) 25 ctrl+ctrl ASO, 31 KO+ctrl ASO, 22 ctrl+SARM1 ASO, and 26 KO+SARM1 ASO, $^{\#\#\#}$p=0.0006. Significant comparison to KO+ctrl ASO group was labeled with $^{\#}$. **(A3-4, B3-4, C3-4)** Velocity of antero- and retrograde transport in

distal axons of ctrl and KO neurons following the treatments indicated in **(A1, B1, C1),** respectively. **(A3-4)** 26-27 ctrl+ctrl ASO, 26-27 KO+ctrl ASO, 29 ctrl+SARM1 ASO, and 32-33 KO+SARM1 ASO. **(B3-4)** 20 ctrl+ctrl ASO, 14-16 KO+ctrl ASO, 14 ctrl+SARM1 ASO, and 20-22 KO+SARM1 ASO, (ctrl+SARM1 ASO vs KO+SARM1 ASO) **p=0.0049, (ctrl+ctrl ASO vs KO+ctrl ASO) **p=0.0022. (C3-4) 24-25 ctrl+ctrl ASO, 16-19 KO+ctrl ASO, 20-22 ctrl+SARM1 ASO, and 22-26 KO+SARM1 ASO, **p= 0.001. One-way or two-way ANOVA with Tukey's multiple comparisons test and Kruskal-Wallis test with Dunn's multiple comparisons test were used; see details in supplemented Excel. All above data represent mean ± SEM, ****p<0.0001, ####p<0.0001. Numbers of independent culture experiments are listed in Sup. Table.

Supplementary Files

This is a list of supplementary files associated with this preprint. Click to download.

- Dataandstatistics20230220.xlsx
- Wholemembrane1.ai
- Mol.ND.supplementarytable20230220.docx
- SupFigures20230509.pdf
- Supplementaryfigurelegends.docx
- Supplementaryvideo.mp4